8-2024

Investigating Near-Field Radiative Heat Transfer with Titanium Carbide MXenes and Slanted Columnar Thin Films

Sean Luke Murray
University of Nebraska-Lincoln, smurraycopelandlan2@huskers.unl.edu

INVESTIGATING NEAR-FIELD RADIATIVE HEAT TRANSFER WITH TITANIUM CARBIDE MXENE AND SLANTED COLUMNAR THIN FILMS

By

Sean Luke Murray

A THESIS

Presented to the Faculty of
The Graduate College at the University of Nebraska
In Partial Fulfillment of Requirements

For the Degree of Master of Science

Major: Mechanical Engineering & Applied Mechanics

Under the Supervision of Professor Mohammad Ghashami

Lincoln, Nebraska
August, 2024

INVESTIGATING NEAR-FIELD RADIATIVE HEAT TRANSFER WITH TITANIUM CARBIDE MXENE AND SLANTED COLUMNAR THIN FILMS

Sean Luke Murray, M. S.

University of Nebraska, 2024

Advisor: Mohammad Ghashami

This work investigates the mechanisms to manipulate and control the magnitudes of Near-Field Radiative Heat Transfer (NFRHT) using two-dimensional materials and nanostructured surfaces. NFRHT occurs when the geometrical features of the radiating objects or the separation distance between interacting bodies are comparable to or lower than the characteristic thermal radiation wavelength. NFRHT magnitudes surpass the blackbody limit by several orders of magnitude due to phenomena such as photon tunneling and new modes of energy transfer, like surface polaritons. Therefore, it is crucial to understand how material properties and surface nanostructures affect NFRHT.

The first part of this work examines the radiative thermal transport between Titanium Carbide MXene surfaces. Samples with varying thicknesses of Titanium Carbide MXene were fabricated using a layer-by-layer spin-coating technique on quartz substrates. Spectroscopic ellipsometry, conducted over a broad spectral range (mid-IR to vacuum ultraviolet), revealed a strong correlation between radiative properties and MXene layer thickness. Further calculations of the spectral and total radiative heat flux between these samples in the near-field regime demonstrated the superior role MXenes can play in controlling radiative heat transfer.

The second part of this study investigates the near-field radiative response of Cobalt-slanted columnar thin films (Co-SCTF) fabricated using glancing angle deposition. Generalized

ellipsometry was used to determine the geometric structure and anisotropic dielectric properties of the nanostructured thin films over the near-IR to mid-IR range. The extracted anisotropic complex dielectric function was used to calculate the NFRHT between the samples. The numerical results show a periodic trend in the magnitudes of NFRHT over an in-plane rotation of the Co-SCTF, with the periodicity varying as the gap distance decreases, allowing better interaction of localized modes from the nanostructures. The NFRHT trend over the gap distance exhibited similar behavior and higher magnitudes than dielectric materials.

ACKNOWLEDGMENTS

First, I extend my deepest thanks to my advisor, Dr. Mohammad Ghashami. His constant support and commitment to excellence have been invaluable in shaping my research experience. I am very grateful to have had him as a mentor, guiding me through the hardships of the research field. I am especially appreciative of his patience, persistence, and the enriching discussions we shared, which enhanced my understanding of both my research and my career aspirations. I would also like to acknowledge Dr. Ufuk Kilic for teaching me about spectroscopic ellipsometry and for his collaborative support on my projects.

I extend my sincere appreciation to the members of my committee, Dr. Nitesh Nama, and Dr. Natale Ianno. Thank you both for your invaluable time and attention to my work, as well as for your insightful career advice that has helped me navigate my professional path.

Additionally, I am deeply thankful for my fellow lab mates: Greg Acosta, Zahra Kamali, Sina Khayam, Chace Franey, and Bakir Al-Ameri. Their continuous support and engaging discussions have created a collaborative and enriching environment that made this journey enjoyable.

I would also like to recognize Dr. Mona Bavarian, Dr. Siamak Nejati, Dr. Suprem Das, Dr. Syed Ibrahim Gnani Peer Mohamed, and Sahand Serajian for their great collaboration. Moreover, I extend my gratitude to Dr. Mathias Schubert and Dr. Eva Schubert for providing access to the spectroscopic ellipsometry instrumentation, which has been crucial for my research.

Lastly, I would like to thank my parents, Ana and Julio Murray, and my sister, Jewell Murray, for their unwavering love, support, and encouragement throughout my academic journey. Your belief in me has been a constant source of motivation, and I am forever grateful for everything you have done.

TABLE OF CONTENT

LIST OF FIGURES

Chapter 1: Introduction

Background in Near-Field Radiative Heat Transfer (NFRHT)

Thermal radiation is a fundamental mode of heat transfer, where energy is emitted by matter in the form of electromagnetic waves. Unlike conduction and convection, thermal radiation does not require a medium for propagation. All objects at a non-zero temperature emit thermal radiation due to thermally driven random oscillations of electric charges within the material [1–4]. A fundamental concept in understanding thermal radiation is the blackbody, an idealized object that absorbs all incident radiation and re-emits energy solely as a function of its temperature. A blackbody in thermal equilibrium emits radiation with a characteristic spectrum described by Planck's Law. Planck's Law [1,4] defines the spectral radiance of a blackbody $B(\lambda, T)$ at a given wavelength λ and temperature T as:

$$B(\lambda, T) = \frac{2hc^2}{\lambda^5} \frac{1}{e^{\frac{hc}{\lambda k_B T}} - 1} \tag{1.1}$$

where, h is Planck's constant (6.626×10^{-34} J · s^{-1}), c is the speed of light in vacuum (299,792,458 m/s), and k_B is Boltzmann's constant (1.3806×10^{-23} J · K^{-1}). This law is fundamental in explaining the spectral density of the radiation emitted by a blackbody in thermal equilibrium at a specific temperature. The intensity of Planck radiation peaks at a wavelength determined by the object's temperature, known as the characteristic thermal wavelength (λ_{th}) [4,5]. Wien's displacement law states that λ_{th} is inversely proportional to the temperature T:

$$\lambda_{th} \cdot T = b \tag{1.2}$$

where b is the Wein's displacement constant (2898 μm · K). For instance, at room temperature (300 K), the characteristic thermal wavelength is approximately ten micrometers ($\approx 10\ \mu m$). The

Stefan-Boltzmann law, derived from Planck's law, states that the total radiative heat power emitted by an object E_{BB} is proportional to the fourth power of its absolute temperature:

$$E_{BB} = \sigma T^4 \tag{1.3}$$

where σ is the Stefan-Boltzmann constant ($5.670 \times 10^{-8}\ \mathrm{W \cdot m^{-2} \cdot K^{-4}}$). This law represents the maximum emissive power, or blackbody limit, for any object at a given temperature. These laws collectively form the basis of far-field radiative heat transfer, which applies under the assumption that the distance d between the emitting surfaces is much larger than the peak wavelengths ($d \gg \lambda_{th}$) [6,7]. However, these laws do not fully represent the heat transfer via thermal radiation when the distance between the interacting objects becomes comparable to or smaller than the characteristic thermal wavelength ($d \leq \lambda_{th}$).

Near-field or nanoscale thermal radiation represents an advanced area within the broader field of thermal radiation, where proximity effects and quantum phenomena significantly alter traditional laws of blackbody radiation. In the far-field, radiative heat transfer is dominated by propagating waves. These waves travel through the medium with an angle of incidence (θ_i) lower than the critical angle (θ_{cr}) of the interface (see Figure 1a). However, when $\theta_i \geq \theta_{cr}$, total internal reflection occurs generating evanescent waves. These waves propagate parallel to the surface with a field amplitude that decays exponentially away from the interface (see Figure 1b). The near-field regime is highly dominated by evanescent waves which increase the energy density of the system [1,8–10]. Evanescent waves are also the result of other energy modes, such as the coupling of electromagnetic waves with oscillating charges on the surface, known as surface polaritons (SP) [1,2,8,9]. These SPs can arise from electromagnetic waves interacting with phonon modes (or dipoles) in dielectric materials, known as surface phonon polaritons (SPhPs).

Electrons can also be excited along the surface of metallic materials due to electromagnetic waves causing surface plasmon polariton (SPP).

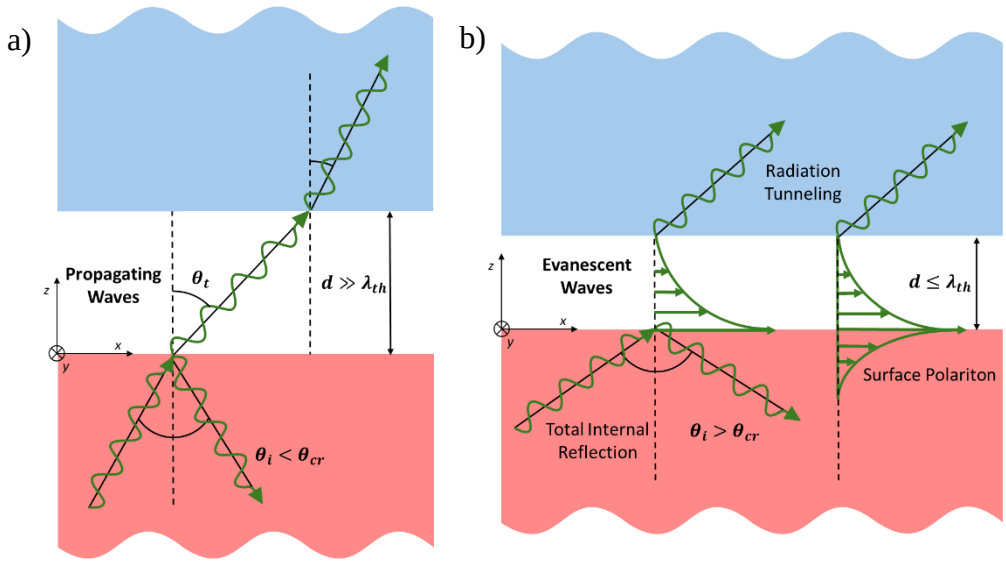

Figure 1: Representation of electromagnetic waves within two semi-infinite media separated by a vacuum gap. (a) Far-field representation where the vacuum gap is larger than the characteristic thermal wavelength. At these distances, propagating waves can travel through a vacuum and reach the other surface. (b) Near-field representation where the gap distance is comparable to or smaller than the characteristic thermal wavelength. At these distances, evanescent waves can be sensed by the other surface.

The theoretical foundation for understanding near-field thermal radiation is grounded in the fluctuation-dissipation theorem (FDT) and fluctuational electrodynamics (FE). FDT explains that thermal emission originates from the random motion of charged particles, creating a fluctuating current [10,11]. This theorem relates the fluctuations in a system to its response to external perturbations. In the context of thermal radiation, FDT describes the stochastic nature of thermal emission at the nanoscale, where the discrete fluctuations of electromagnetic fields become significant [8]. Combining FDT with Maxwell's electromagnetic wave theory, FE can describe both far-field and near-field thermal radiation phenomena. This framework considers the electromagnetic field fluctuations generated by thermally induced dipoles within a material and how these fields propagate and interact.

NFRHT with 2D Materials and Nanostructures

In recent years, researchers have demonstrated that NFRHT between polar dielectric materials can exceed the blackbody limit by several orders of magnitude. These groundbreaking findings are now driving the search for the best combinations of materials to maximize and control NFRHT. Consequently, researchers are exploring the use of two-dimensional (2D) materials, such as graphene [12–14], black phosphorus [15,16], hexagonal boron nitride [12,15], and transition metal dichalcogenides (TMDs) [17,18], for near-field thermal radiation. These materials possess unique electronic, thermal, and optical properties that can be leveraged to enhance and control thermal radiation at the nanoscale [19,20].

Several groups have investigated the effects of monolayers of graphene-coated on dissimilar materials as a way to alter the optical properties of their systems. Lim et al. [21] investigated the effects of monolayers of graphene-coated on doped Si plates. The optical constants of p-type doped Si highly depend on the doping concentration and temperature, meaning that at different conditions, a mismatch in the SPPs modes may exist that dominates the radiative heat transfer rates. To better match these resonant modes, they proposed to use a monolayer of graphene with its chemical potential as a tuning parameter. They were able to achieve up to two orders of magnitude enhancement using a monolayer of graphene-coated on both surfaces with a chemical potential of $\mu = 0.3$ eV and a p-type doping concentration of $10^{17}\mathrm{cm}^{-3}$ for both the source and receiver. Similarly, others have successfully been able to use a combination of surfaces coated with monolayers of graphene to modulate the magnitudes of NFRHT [22–24].

Similarly, researchers have used a monolayer of black phosphorus (BP). In this case, Ge et al. [25] investigate the effects between two suspended black phosphorus sheets. They determined

that the radiative heat flux can exceed the blackbody limit over 2 to 4 orders of magnitude for separation distances between 10 nm to 100 nm. They attributed this enhancement to the excitation of anisotropic and hyperbolic SPP modes. Adding to this, due to the anisotropic behavior of BP, they were able to demonstrate a large thermal modulation based on the twisted angle of principal axes between the BP sheets. These anisotropic thermal and optical properties enable direction-dependent control of radiative heat transfer, which can be advantageous in designing thermal rectifiers or directional thermal emitters [16,26].

As stated before, the implementation of 2D materials has expanded the field of materials considered for near-field thermal radiation applications due to their unique optical properties such as tunable optical absorption, tunable bandgaps, and support of polaritonic modes [13,15,16]. Their high thermal conductivity and tunable emissivity offer solutions for efficient heat dissipation in electronic devices, while their strong light-matter interactions and ability to support surface polaritons lead to improved sensitivity and resolution in near-field thermal imaging [27,28]. Although these materials are strong candidates, researchers have been delving deeper, using nanofabrication techniques to develop engineered surfaces to better tailor these effects. Metasurfaces and nanostructures offer a higher degree of design flexibility, scalability, material versatility, and ease of integration [29,30]. These advantages can simplify the development and deployment of advanced thermal radiation technologies, making them a potentially more practical and efficient choice for many applications [29–32].

The exploration of near-field thermal radiation has significantly advanced with the advent of metasurfaces and nanostructures such as 1D or 2D nanoarrays, nanogratings, and multilayer structures. These engineered structures manipulate electromagnetic waves at sub-wavelength scales, leading to a better and more controlled manipulation of their thermal radiative properties.

In addition to creating these new surfaces, researchers are discovering new polaritonic modes, like localized surface modes, that improve the coupling of resonant modes inherent to the materials used [33,34].

Fernández-Hurtado et al. [35], have shown that metasurfaces of doped Si featuring 2D periodic arrays of holes can achieve higher NFRHT magnitudes than smooth Si and SiO_2 surfaces. The fundamental mechanisms behind this behavior are the presence of broadband SPPs in doped silicon and the ability to modify the dispersion relation of these SPPs through nanostructuring. Besides the enhancement feature, they could show the tunability capacities of these metasurfaces. The peak of spectral heat transfer coefficient (HTC) shifts to longer wavelengths as the size of the holes increases. This provides additional evidence supporting the main concept of designing metasurfaces to precisely adjust their thermal radiative properties.

As an alternative nanofabrication method, researchers have experimented with incorporating multilayer systems to increase the number of surface modes available for heat transfer due to the multiple surfaces. Iizuka et. al [36], examine the effects of a multilayer structure composed of a lossless dielectric material and a lossy material unit cell with a smaller periodicity than the relevant thermal wavelength. They demonstrated a 40-fold increase in performance compared to a bulk system, primarily due to additional surface states that act as intermediaries, allowing surfaces distant from the central gap to participate in heat transfer. In other words, the enhancement arises from the increase in available surface modes facilitated by the multilayer structure.

Applications of NFRHT using 2D materials and nanostructures leverage their unique properties to enhance and control thermal radiation for various technological advancements. On one side, 2D materials contribute with their unique intrinsic properties, such as the ability to support

polaritonic modes within the mid-infrared range, bandgap tunability, and 2D anisotropic properties [37–41]. On the other side, the versatility and customizability of nanostructures can better manipulate their properties, such as spectral thermal emission, and the support of tunable resonant modes along induced anisotropic properties [29,30,42–44]. Enhanced and tunable radiative heat transfer provides more effective thermal management solutions for electronic devices. Additionally, precise control over emission spectra and directionality is critical for developing high-performance thermal sensors and imaging technologies [29,30]. These advancements are essential for pushing the boundaries of current technological capabilities and driving innovation in energy, electronics, and sensing applications.

Objective of the Thesis

Researchers are continually pushing the boundaries of material capabilities to further enhance the control over the magnitudes and spectra of NFRHT. Consequently, this thesis aims to introduce MXenes, a new family of 2D materials that exhibit promising characteristics such as tunable optical properties and thickness-dependent characteristics. Thus, the first objective of this thesis is to theoretically examine the NFRHT behavior of Titanium Carbide ($Ti_3C_2T_x$) MXene. This research aims to explore the potential of MXenes in manipulating NFRHT, thereby paving the way for future applications of this novel material in advanced thermal management and energy conversion systems.

Numerous nano-engineered surfaces have been studied for NFRHT, showing promising manipulative modes that can adjust the behavior and magnitudes of heat transfer. So far, some of the nano-engineered surfaces studied have been multilayer media, 1D- and 2D-nanogratings, nanoholes, and rough surfaces while there are more nanofabrication techniques available to

create these metasurfaces. Among these different nanofabrication technologies is a physical vapor deposition process called glancing angle deposition (GLAD). This technique has been used to grow self-organized highly spatially coherent 3D geometries at the nanoscale. This technique has a high impact on applications in the fields of photonics, nanosensors, and plasmonics. Metasurfaces via GLAD have yet to be investigated in the field of NFRHT. Therefore, the second objective of this thesis is to examine the anisotropic near-field radiative response of slanted columnar thin films using an experimentally extracted optical constant via generalized spectroscopic ellipsometry and best-match physical models.

Organization of the Thesis

This thesis has the following structure:

- Chapter 1 presents the theoretical background of NFRHT calculations. This chapter introduces the basis of fluctuational electrodynamics and fluctuational electrodynamics to interpret the near-field phenomenon. This is followed by the description of the analytical method used to calculate NFRHT via dyadic Green's function. The scattering matrix method for 1D-layered isotropic media and the modified 4×4 transfer matrix method for anisotropic media is also included.
- Chapter 2 presents a numerical analysis of NFRHT using Titanium Carbide MXene. The state-of-the-art NFRHT calculation is used for simple structure configurations while the scattering matrix method is used for multilayer media to better display its performance. The chapter presents the impact of this new 2D material and its potential to enhance the magnitudes of NFRHT between materials.

- Chapter 3 presents the idea of NFRHT modulation via anisotropic nanostructures made of Cobalt slanted columns fabricated via glancing angle deposition. The 4×4 enhanced transfer matrix method is used to describe the NFRHT dependency on the sample orientation. The chapter presents the effects of NFRHT modulation due to engineered anisotropic features using columnar nanostructures.

Chapter 2: Formulation of Near-Field Radiative Heat Transfer

Stochastic Maxwell equations and fluctuational electrodynamics.

The foundation of fluctuational electrodynamics (FE) is the fluctuation-dissipation theorem (FDT), in which thermal radiation originated [11]. Electromagnetic fields are generated by the out-of-phase oscillations of charges of opposite signs (dipoles) [1,2,8]. When a medium is above 0 K, thermal agitation causes chaotic movement of charged particles, creating oscillating dipoles. These dipoles generate a fluctuating electromagnetic field, known as the thermal radiation field, which comes from random thermal motion [8]. From a big-picture perspective, the thermal radiation field can be considered an electromagnetic field created by large-scale fluctuating currents. The FE framework relies on this macroscopic view, adding fluctuating currents to Maxwell's equations to model the thermally generated electromagnetic field. FE helps us calculate the spectral density of thermal radiation in the near-field regime and is crucial for modeling radiative heat transfer between closely spaced objects [1,4,10].

Heat transfer happens between bodies at different temperatures. A central assumption of FE is that current fluctuations are defined only by the FDT at the local thermodynamic temperature and do not depend on incoming radiation from other objects. In simple terms, the theory works for any media in local thermodynamic equilibrium, where you can define an equilibrium temperature at any point within the body at any time. FE is essential for solving near-field radiation heat transfer issues because it enables the calculation of thermal emission using Maxwell's equations, which generally only describe the propagation of electromagnetic waves.

The Maxwell equations are expressed as follows [1,8,10]:

$$\nabla \times \boldsymbol{E}(\boldsymbol{r}, \boldsymbol{\omega}) = i\omega\mu_0 \boldsymbol{H}(\boldsymbol{r}, \omega) \tag{2.1}$$

$$\nabla \times \boldsymbol{H}(\boldsymbol{r}, \omega) = -i\omega\varepsilon(\omega)\varepsilon_0 \boldsymbol{E}(\boldsymbol{r}, \omega) + \boldsymbol{J}^{fl}(\boldsymbol{r}, \omega) \tag{2.2}$$

$$\nabla \cdot \boldsymbol{E}(\boldsymbol{r}, \omega) = 0 \tag{2.3}$$

$$\nabla \cdot \boldsymbol{H}(\boldsymbol{r}, \omega) = 0 \tag{2.4}$$

where with the assumption that the materials are non-magnetic. Electromagnetic fields have the form $e^{-i\omega t}$. The term $\boldsymbol{J}^{fl}$ corresponds to a fluctuating current density due to electric dipole oscillations, which is added to the right-hand side of equation (2.2). This random variable is fully defined by its first two moments [8,10]. The first moment is its ensemble average, which is zero. This means the average thermally radiated electromagnetic fields are also zero. The second moment represents the ensemble average of the spatial correlation function for the fluctuating current, is given by the fluctuation-dissipation theorem [11]:

$$\langle J_\alpha^{fl}(\boldsymbol{r}', \boldsymbol{\omega}) J_\beta^{fl^*}(\boldsymbol{r}'', \boldsymbol{\omega}') \rangle = \frac{4\omega\varepsilon_0\varepsilon''(\omega)}{\pi} \Theta(\omega, T)\delta(\boldsymbol{r}' - \boldsymbol{r}'')\delta(\omega - \omega')\delta_{\alpha\beta} \tag{2.5}$$

where $\langle\ \rangle$ denotes an ensemble average, the superscript * refers to complex conjugate, α, and β are orthogonal components indicating the state of polarization of the fluctuating current, $\delta(\boldsymbol{r}' - \boldsymbol{r}'')$ and $\delta(\omega - \omega')$ are Dirac functions, while $\delta_{\alpha\beta}$ is the Kronecker function. The terms $\Theta(\omega, T)$ is the mean energy of an electromagnetic state at frequency ω and temperature *T*

$$\Theta(\omega, T) = \frac{\hbar\omega}{\exp(\hbar\omega/k_B T) - 1} \tag{2.6}$$

where k_B is the Boltzmann constant and $\hbar$ is the reduced Planck constant. The fluctuation-dissipation theorem is limited to the following assumptions: the media are linear, isotropic, non-magnetic, and defined by a dielectric function local in space. In addition, the fluctuation-

dissipation is applicable when the media are in local thermodynamic equilibrium, where an equilibrium temperature *T* can be defined.

FE is a thorough framework that considers all near-field effects, including evanescent modes. Moreover, it aligns with the classical theory of thermal radiation when the sizes of the bodies and their distances apart are greater than the characteristic thermal wavelength [10].

Dyadic Green's Function (DGF)

For a known temperature and specific geometric features, Maxwell's equations need to be solved to obtain the electric and magnetic field distributions. This can be achieved using the dyadic Green's function, which simplifies and compacts the formulations. With the dyadic Green's function, the induced electric and magnetic fields from the fluctuating current density can be represented as volume integrals in the frequency domain [1,8,10]:

$$\boldsymbol{E}(\boldsymbol{r},\boldsymbol{r}',\omega) = i\omega\mu_0 \int_V dV' \overline{\overline{\boldsymbol{G}}}^E(\boldsymbol{r},\boldsymbol{r}',\omega)\cdot\boldsymbol{J}^{fl}(\boldsymbol{r}',\omega) \tag{2.7}$$

$$\boldsymbol{H}(\boldsymbol{r},\boldsymbol{r}',\omega) = \int_V dV' \overline{\overline{\boldsymbol{G}}}^M(\boldsymbol{r},\boldsymbol{r}',\omega)\cdot\boldsymbol{J}^{fl}(\boldsymbol{r}',\omega) \tag{2.8}$$

Equations (2.7-8) give the electric and magnetic field observed in a medium of volume *V* due to a current density vector $\boldsymbol{J}^{fl}$ located at $\mathbf{r}'$ in a source medium of volume V'.

In heat transfer calculation, one is interested in calculating the radiative heat flux exchanged by the bodies instead of the electric and magnetic fields. The Poynting vector gives the instantaneous energy flux carried by a wave as a function of the electric and magnetic fields. The emitted energy flux can be expressed by the ensemble average of the Poynting vector,

$$\langle \boldsymbol{S}(\boldsymbol{r},\omega)\rangle = \frac{1}{2} Re\{\langle \boldsymbol{E}(\boldsymbol{r},\omega) \times \boldsymbol{H}^{*}(\boldsymbol{r},\omega)\rangle\} \tag{2.9}$$

represents the monochromatic radiative heat flux. Calculation of the radiative heat flux requires the cross-spectral density of electric and magnetic field vectors expressed in equations (2.7-8) shown as follows:

$$\begin{aligned} &\langle \boldsymbol{E}_x(\boldsymbol{r},\omega) \times \boldsymbol{H}_y{}^{*}(\boldsymbol{r},\omega)\rangle \\ &= i\omega\mu_0 \int_V dV' \int_V dV'' \, \boldsymbol{G}^{E}_{x\alpha}(\boldsymbol{r},\boldsymbol{r}',\omega)\boldsymbol{G}^{H^*}_{y\beta}(\boldsymbol{r},\boldsymbol{r}',\omega)\,\langle J^{fl}_{\alpha}(\boldsymbol{r}',\boldsymbol{\omega})J^{fl^*}_{\beta}(\boldsymbol{r}'',\boldsymbol{\omega}')\rangle \end{aligned} \tag{2.10}$$

$$\begin{aligned} &\langle \boldsymbol{E}_y(\boldsymbol{r},\omega) \times \boldsymbol{H}_x{}^{*}(\boldsymbol{r},\omega)\rangle \\ &= i\omega\mu_0 \int_V dV' \int_V dV'' \, \boldsymbol{G}^{E}_{y\alpha}(\boldsymbol{r},\boldsymbol{r}',\omega)\boldsymbol{G}^{H^*}_{x\beta}(\boldsymbol{r},\boldsymbol{r}',\omega)\,\langle J^{fl}_{\alpha}(\boldsymbol{r}',\boldsymbol{\omega})J^{fl^*}_{\beta}(\boldsymbol{r}'',\boldsymbol{\omega}')\rangle \end{aligned} \tag{2.11}$$

where α and β represent the orthogonal components indicating the polarization state of the fluctuating current. Substitution of the FDT (equation 2.5) into equations (2.10-11) provides an explicit expression relating the monochromatic radiative heat flux to the local temperature T_s of the heat source at z' along the z-direction

$$q_{\omega}(z') = \frac{2k_0^2\Theta(\omega,T_s)}{\pi} \int_V Re\left\{ i\varepsilon_s''(\omega) \begin{bmatrix} \boldsymbol{G}^{E}_{x\alpha}(\boldsymbol{r},\boldsymbol{r}',\omega)\boldsymbol{G}^{H^*}_{y\beta}(\boldsymbol{r},\boldsymbol{r}',\omega) \\ -\boldsymbol{G}^{E}_{y\alpha}(\boldsymbol{r},\boldsymbol{r}',\omega)\boldsymbol{G}^{H^*}_{x\beta}(\boldsymbol{r},\boldsymbol{r}',\omega) \end{bmatrix} \right\} dV' \tag{2.12}$$

here, $\varepsilon_s''(\omega)$ is the imaginary part of the dielectric function of the heat source [45].

Since the dyadic Green's function depends on the geometry of the physical system, the following sections will briefly describe the dyadic Green's functions for two representative structures, i.e., for two semi-infinite media and multilayered media.

Weyl's representation of the DGF for isotropic media

Let's consider a one-dimensional layered medium, as represented by Figure 2. The complex wavevector for an arbitrary layer-*l* is defined as $\boldsymbol{k}_l$ with $\boldsymbol{k}_l^2 = \varepsilon_l k_0^2$ where $k_0 = \omega/c_0$ is the wavevector in a vacuum. Here, c_0 is the speed of light in vacuum and ω is the angular frequency. A cylindrical coordinate system is utilized for the space variable $\boldsymbol{r} = \rho\hat{\boldsymbol{\rho}} + z\hat{\boldsymbol{z}}$, where the ρ-direction is parallel to the interface and the z-direction (propagation direction) is perpendicular to the interface. Thus, $\boldsymbol{k}_l = k_\rho\hat{\boldsymbol{\rho}} + k_{zl}\hat{\boldsymbol{z}}$ and $k_{zl} = \sqrt{\boldsymbol{k}_l^2 - k_\rho^2} = \sqrt{\varepsilon_l k_0^2 - k_\rho^2}$, where k_ρ is the magnitude of the in-plane component that is always a real value and the k_{zl} is the magnitude in the propagation direction. Since only real and positive frequencies (ω) are considered, k_0 is always positive and real. Following the rules for electromagnetic waves propagating along interfaces, the amplitude parallel to the interface must not change, meaning that k_ρ is always real. Therefore, the magnitude of the wavevector along the propagation direction, $k_{zl} = \sqrt{\varepsilon_l k_0^2 - k_\rho^2}$, will be real when $0 \le k_\rho \le \omega/c_0$ and purely imaginary when $k_\rho > \omega/c_0$.

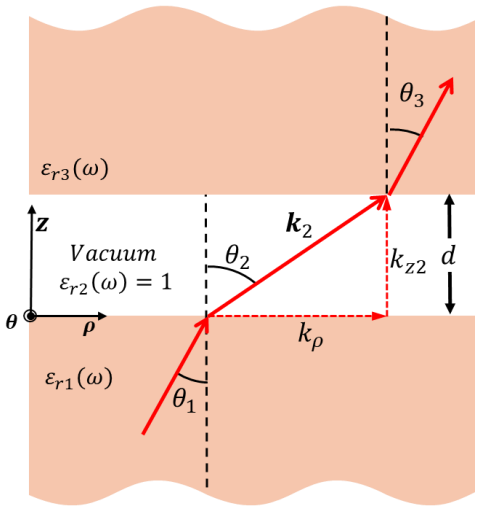

Figure 2: Illustration of the plane wave propagating through a system of two semi-infinite bodies separated by a vacuum gap distance d.

To convert radiative heat flux into a one-dimensional geometry, the dyadic Green's functions can be expressed as an integral of plane waves using the Weyl representation:

$$\overline{\overline{\boldsymbol{G}}}^{E,H}(\boldsymbol{r},\boldsymbol{r}',\omega) = \int_{-\infty}^{\infty} \frac{d\boldsymbol{k}_\rho}{4\pi^2}\,\overline{\overline{\boldsymbol{g}}}^{E,H}\left(\boldsymbol{k}_\rho, z_c, z', \omega\right) e^{i\boldsymbol{k}_\rho(\boldsymbol{R}-\boldsymbol{R}')} \tag{2.13}$$

where $d\boldsymbol{k}_\rho = dk_x dk_y$, z' is the location of the source layer, $\overline{\overline{\boldsymbol{g}}}^{E,H}$ is the Weyl component of the dyadic Green's function, $\boldsymbol{R}$, and $\boldsymbol{R}'$ are the parallel and perpendicular components of the position vectors of the observation and source points, respectively. Substitution of equation (2.13) into equation (2.4) in polar coordinates gives the monochromatic radiative heat flux at z_c along the z-direction in terms of the Weyl components of the dyadic Green's function [45]:

$$\begin{aligned} q_\omega(z_c) &= \frac{k_0^2\Theta(\omega,T_s)}{\pi^2} \\ &\times Re\left\{ i\varepsilon_s''(\omega)\int_0^\infty k_\rho dk_\rho \int_z dz' \begin{bmatrix} g_{\rho\alpha}^E(k_\rho,z_c,z',\omega)\,g_{\theta\alpha}^{H^*}(k_\rho,z_c,z',\omega) \\ -g_{\theta\alpha}^E(k_\rho,z_c,z',\omega)\,g_{\rho\alpha}^{H^*}(k_\rho,z_c,z',\omega) \end{bmatrix} \right\} \end{aligned} \tag{2.14}$$

where α involves the summation over the three orthogonal components. This is the representation of the contributions of both, propagating and evanescent waves, i. e. $q_\omega(z_c) = q_\omega^{prop}(z_c) + q_\omega^{evan}(z_c)$. An explicit expression has been derived to separate the contributions of propagating waves and evanescent waves to the spectral heat flux, respectively [10,46]:

$$q_{\omega,13}^{prop}(z_c) = \frac{[\Theta(\omega,T_1)-\Theta(\omega,T_3)]}{4\pi^2}\int_0^{k_0} k_\rho \cdot \boldsymbol{Z}_{13}^{prop} dk_\rho \tag{2.15}$$

$$q_{\omega,13}^{evan}(z_c) = \frac{[\Theta(\omega,T_1)-\Theta(\omega,T_3)]}{\pi^2}\int_{k_0}^{k_\infty} k_\rho \cdot \boldsymbol{Z}_{13}^{evan} \cdot e^{-2k_{z2}''d} dk_\rho \tag{2.16}$$

As seen in equation (2.16), the near-field effects due to the evanescent modes are clearly represented by the exponentially decaying term $e^{-2k''_{z2}d}$. The terms $\boldsymbol{Z}_{13}^{prop}$ and $\boldsymbol{Z}_{13}^{evan}$ are the exchange functions or energy transmission coefficients that represent the probability of energy transfer due to propagating modes and evanescent waves (photon tunneling). These probabilities are expressed as follows:

$$\boldsymbol{Z}_{13}^{prop} = \sum_{\gamma=TE,TM} \frac{(1-\left|r_{21}^{\gamma}\right|^2)(1-\left|r_{23}^{\gamma}\right|^2)}{|1-r_{21}^{\gamma}r_{23}^{\gamma}e^{2ik_{z2}d}|^2} \tag{2.17}$$

$$\boldsymbol{Z}_{13}^{evan} = \sum_{\gamma=TE,TM} \frac{\mathrm{Im}(r_{21}^{\gamma})\mathrm{Im}(r_{23}^{\gamma})}{|1-r_{21}^{\gamma}r_{23}^{\gamma}e^{2ik_{z2}d}|^2} \tag{2.18}$$

From equation (2.17), representing the propagating waves, the term $1-\left|r_{2j}^{\gamma}\right|^2 = 1-\rho_{\omega,2j}^{\prime\gamma} = \alpha_{\omega}^{\prime\gamma}$ can be seen as the spectral absorptance of layer j where $\rho_{\omega,2j}^{\prime\gamma}$ is the spectral reflectivity. Following Kirchhoff's Law of thermal radiation, the spectral absorptance is equal to the spectral emissivity i.e., $\alpha_{\omega}^{\prime\gamma} = \tilde{\varepsilon}_{\omega}^{\prime\gamma}$. Therefore, these terms describe the spectral far-field emissivity of the source emitting layer and the spectral far-field absorptivity of the receiving absorbing layer. Similarly, for the evanescent waves shown in equation (2.18), the terms $\mathrm{Im}(r_{2j}^{\gamma})$ represent the near-field spectral emissivity and absorptivity [8,47]. The denominator of equations (2.17-18) has a Fabry-Perot resonator as it accounts for the wave interference and multiple reflections of the configuration.

Field amplitudes via S-Matrix

Figure 3 will be used to better represent the general form to calculate the spectral radiative heat flux emitted from a source layer of defined thickness $z_{s+1} - z_s$ at a point z_c in layer l is given as [45]:

$$q_{\omega,sl}(z_c) = \frac{k_0^2 \Theta(\omega, T_s)}{\pi^2}$$

$$\times Re\left\{ i\varepsilon_s''(\omega) \int_0^{\infty} k_\rho dk_\rho \int_{z_s}^{z_{s+1}} dz' \begin{bmatrix} g_{sl\rho\rho}^E(k_\rho, z_c, z', \omega) g_{sl\theta\rho}^{H^*}(k_\rho, z_c, z', \omega) \\ +g_{sl\rho z}^E(k_\rho, z_c, z', \omega) g_{sl\theta z}^{H^*}(k_\rho, z_c, z', \omega) \\ -g_{sl\theta\theta}^E(k_\rho, z_c, z', \omega) g_{sl\rho\theta}^{H^*}(k_\rho, z_c, z', \omega) \end{bmatrix} \right\} \quad (2.19)$$

where $g_{sl\rho\rho}^E g_{sl\theta\rho}^{H^*} + g_{sl\rho z}^E g_{sl\theta z}^{H^*}$ represents a function to correlate the TM-polarized waves from the source point z' to z_c and $g_{sl\theta\theta}^E g_{sl\rho\theta}^{H^*}$ for TE-polarized waves.

For this case, the source layer emits waves in the forward (z-positive) and backward (z-negative) directions from point z' within the source layer *s*. The energy emitted from the source layer *s* is represented as the contribution of the multiple points within z_s to z_{s+1}. The radiative heat flux calculated at z_c is the sum of the contribution of all the multiple points within layer *s*.

The field amplitudes within each layer are the result of multiple reflections within the interfaces. The coefficients *A* and *B* represent the amplitudes of waves traveling forward and backward, respectively, as the result of the forward emission of the source layer. Likewise, the coefficients *C* and *D* represent the amplitudes of waves traveling forward and backward, respectively, as the result of the backward emission of the source layer.

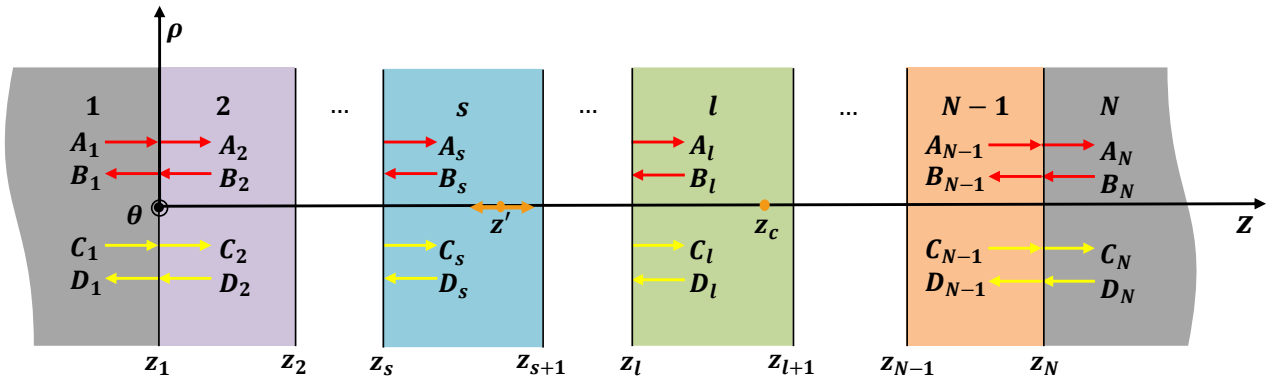

Figure 3: One-dimensional layered media representation with their corresponding field amplitudes due point (z') in the source layer (s) emitting in the forward and backward directions. The radiative heat flux is calculated at a point (z_c) in layer l.

The coefficients A_l, B_l, C_l, and D_l for an arbitrary layer "*l*" can be found using the transfer matrix (T-matrix) method [48]. Numerical instabilities have been found when employing the T-matrix for NFRHT calculations due to the out-of-scale values for the wavevector. This instability has been controlled using a modified version of the T-matrix called the scattering matrix (S-matrix). The idea of the S-matrix is to calculate separately the outgoing and incoming wave amplitudes in each interface to mitigate the instabilities [45,49,50]. The coefficients can be found separately for the forward-emitting (A_l and B_l) and backward-emitting (C_l and D_l). For the analysis, let's only consider A_l and B_l. The coefficients for the semi-infinite media *1* and *l* are related using the following S-matrix:

$$\begin{bmatrix} A_l \\ B_1 \end{bmatrix} = S(1,l) \begin{bmatrix} A_1 \\ B_l \end{bmatrix} \tag{2.19}$$

where $S(1,l)$ is the 2×2 S-matrix between layers 1 to l. The coefficients for each layer are calculated using consecutive relationships between layers. Using the definition of the T-matrix in terms of the incoming and outgoing wave amplitudes, the components of the 2×2 S-matrix for the next layers are expressed as follows:

$$S_{11}(1,l+1) = \frac{S_{11}(1,l)t_{l,l+1}e^{ik_{zl}t_l}}{1 - S_{12}(1,l)r_{l,l+1}e^{2ik_{zl}t_l}} \tag{2.20}$$

$$S_{12}(1,l+1) = \frac{S_{12}(1,l)e^{2ik_{zl}t_l} - r_{l,l+1}}{1 - S_{12}(1,l)r_{l,l+1}e^{2ik_{zl}t_l}} \tag{2.21}$$

$$S_{21}(1,l+1) = \frac{S_{11}(1,l+1)S_{22}(1,l)r_{l,l+1}e^{ik_{zl}t_l}}{t_{l,l+1}} + S_{21}(1,l) \tag{2.22}$$

$$S_{22}(1,l+1) = \frac{S_{22}(1,l)\left[r_{l,l+1}S_{12}(1,l+1)+1\right]e^{ik_{zl}t_l}}{t_{l,l+1}} \tag{2.23}$$

where $t_{l,l+1}$is the Fresnel's transmission coefficient and $r_{l,l+1}$is the Fresnel's reflection coefficient, and t_l is the thickness of the layer l. The initial values for the S-matrix components, regardless of what the initial layer will start using the following values:

$$\begin{bmatrix} S_{11}(1,1) & S_{12}(1,1) \\ S_{21}(1,1) & S_{22}(1,1) \end{bmatrix} = \begin{bmatrix} 1 & 0 \\ 0 & 1 \end{bmatrix} \tag{2.24}$$

For better representation, here is the scattering matrix of the initial fields across the interface of layer 1 and 2 where the variable $l = 1$. Here, $S(1,2)$ is represented as:

$$\begin{bmatrix} S_{11}(1,2) & S_{12}(1,2) \\ S_{21}(1,2) & S_{22}(1,2) \end{bmatrix} = \begin{bmatrix} t_{12} & r_{21} \\ r_{12} & t_{21} \end{bmatrix} \tag{2.25}$$

Note: The thickness of the layer seen in the exponential term on equation (2.20-23) is assumed to be zero for adjacent layers as this represents the interaction between the interfaces. As seen in equation (2.25), the diagonal terms describe the transmission through the interface while the off-diagonal terms describe the interface's reflection coefficients.

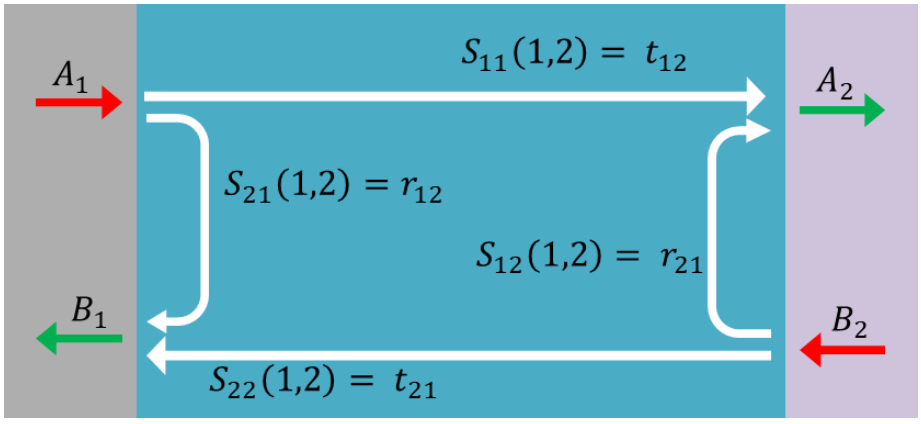

Figure 4: Representation of the scattering matrix elements between layers 1 and 2. The incoming and outgoing waves to the interface are represented with green and red arrows, respectively.

The representation shown in Figure 4 clearly shows the interaction between the incoming and outgoing waves through the S-matrix across the interface of layer 1 and 2:

$$\begin{aligned} A_2 &= t_{12}A_1 + r_{21}B_2 \\ B_1 &= r_{12}A_1 + t_{21}B_2 \end{aligned} \quad \Rightarrow \quad \begin{bmatrix} A_2 \\ B_1 \end{bmatrix} = S(1,2) \begin{bmatrix} A_1 \\ B_2 \end{bmatrix} \tag{2.26}$$

Calculation for the field amplitudes

For the NFRHT calculations in this work, there is no external source of energy. Therefore, the coefficients corresponding to external waves, as seen in Figure 5, will be set to zero, meaning $A_1 = C_1 = B_N = D_N = 0$.

Emitting Thin Film

As seen in Figure 5, layer s emits waves of unit amplitude in both forward and backward directions. First, let's consider the coefficients A_l and B_l for the source layer when emitting in the forward direction. Considering the layers 1, s, and N, there are four unknowns which are B_1, A_s, B_s and A_N. To determine these field amplitudes, there are two relationships to make via the S-matrix: between layers 1 and s, and between layers s and N.

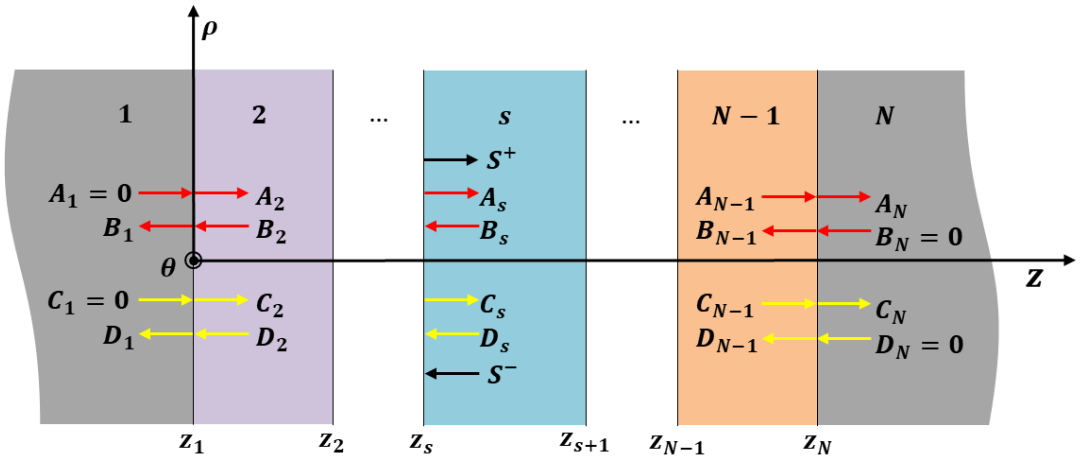

Figure 5: Representation for an emitting thin film.

The relationship between layer 1 and s is given as follows:

$$A_s = S_{12}(1, s)B_s \tag{2.27}$$

$$B_1 = S_{22}(1, s)B_s \tag{2.28}$$

The relationship between layer s and N is given as follows:

$$\begin{bmatrix} A_N \\ B_s \end{bmatrix} = \begin{bmatrix} S_{11}(s,N) & S_{12}(s,N) \\ S_{21}(s,N) & S_{22}(s,N) \end{bmatrix} \begin{bmatrix} A_s + S^+ \\ 0 \end{bmatrix} \quad \Rightarrow \quad \begin{matrix} A_N = S_{11}(s,N)(A_s + S^+) \\ B_s = S_{21}(s,N)(A_s + S^+) \end{matrix} \tag{2.29}$$

When determining the coefficients of layer N, the presence of the emitting source layer s must be considered, as layer N is located at a position z greater than z'. The amplitude of the source at the boundary z_s in layer s is given by $S^+ = e^{ik_{zs}t'_{s,+}}$ where $t'_{s,+} = z_{s+1} - z_s$. Combining equations (2.27) and (2.29) results in:

$$B_s = \frac{S_{21}(s,N)S^+}{1 - S_{21}(s,N)S_{12}(1,s)} \tag{2.30}$$

Starting with equation (2.30), the coefficients for forward emitting fields in layers 1, s, and N can be found. Now, let's consider the coefficients D_l and C_l for the source layer when emitting in the backward direction. Similar to the forward emitting scenario, there are four unknowns which are D_1, C_s, D_s and C_N. The field amplitudes can be determined with the S-matrix between layer 1 and s, layers s and N.

The relationship between layer 1 and s is given as follows:

$$\begin{bmatrix} C_s \\ D_1 \end{bmatrix} = \begin{bmatrix} S_{11}(1,s) & S_{12}(1,s) \\ S_{21}(1,s) & S_{22}(1,s) \end{bmatrix} \begin{bmatrix} 0 \\ D_s + S^- \end{bmatrix} \quad \Rightarrow \quad \begin{matrix} C_s = S_{12}(1,s)(D_s + S^-) \\ D_1 = S_{22}(1,s)(D_s + S^-) \end{matrix} \tag{2.31}$$

When determining the coefficients of layer 1, the presence of the emitting source layer s must be considered, as layer 1 is located at a position z lower than z'. The amplitude of the source at the boundary z_s in layer s is given by $S^- = e^{ik_{zs}t'_{s,-}}$ where $t'_{s,-} = z_s - z_{s+1}$. The relationship of the amplitude fields between layers s and N are given as follows:

$$C_N = S_{11}(s,N)C_s \tag{2.32}$$

$$D_s = S_{21}(s,N)C_s \tag{2.33}$$

Using equations (2.31) and (2.33) gives:

$$C_s = \frac{S_{12}(1,s)S^-}{1 - S_{12}(1,s)S_{21}(s,N)} \tag{2.34}$$

The coefficients for the backward emitting fields in layers 1, s, and N can be found starting with equation (2.33).

Emitting Semi-Infinite Medium

The formulation becomes simpler when using a semi-infinite emitting source. Assuming that the emitting semi-infinite media is layer 1, then all C_l and D_l coefficients are zero due to no emitting waves in the backward direction from the source layer.

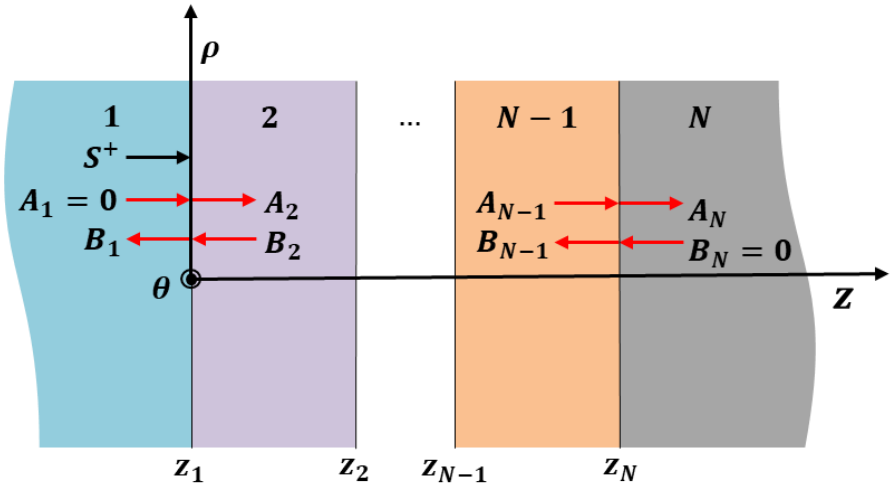

Figure 6: Representation for an emitting semi-infinite medium.

Then, considering layers 1 and N as shown in Figure 6, there are just two unknown fields to find (B_1 and A_N) that can be determined using the S-matrix relation between layers 1 and N:

$$\begin{bmatrix} A_N \\ B_1 \end{bmatrix} = \begin{bmatrix} S_{11}(1,N) & S_{12}(1,N) \\ S_{21}(1,N) & S_{22}(1,N) \end{bmatrix} \begin{bmatrix} S^+ \\ 0 \end{bmatrix} \quad \Rightarrow \quad \begin{matrix} A_N = S_{11}(1,N) \\ B_1 = S_{21}(1,N) \end{matrix} \tag{2.35}$$

where the amplitude of the emitting semi-infinite medium is $S^+ = 1$. For more details on the algorithm needed to calculate the NFRHT problem using the S-matrix approach, see Ref. [45].

Weyl components of the DGF

Emitting Thin Film

Equation (2.19) has an integration over the volume of the emitting body which has a finite thickness of $t_s = z_{s+1} - z_s$, therefore, the limits of integration for the upper and lower boundaries are: $z_{s+1} = t_s$ and $z_s = 0$, respectively. This integration has been performed analytically over the Weyl components at $z_c = z_l$ with respect to z' present in Ref. [47]. It is important to mention that while this integration can be performed numerically, it comes with the downside of increasing the necessary computational time [45]. The representation of the Weyl components of the DGF has been simplified for the cases used in this work.

The Weyl component of the DGF for a film emitter in terms of TM- and TE-polarization, respectively:

$$g^{E}_{sl\rho\rho} g^{H^*}_{sl\theta\rho}\left(k_\rho, z_c = z_l, \omega\right) + g^{E}_{sl\rho z} g^{H^*}_{sl\theta z}\left(k_\rho, z_c = z_l, \omega\right)$$

$$= \frac{ik_{zl}k_l^*}{8k'_{zs}k''_{zs}k_l|k_s|^2|k_{zs}|^2} \times \begin{bmatrix} k'_{zs}(e^{2k''_{zs}t_s} - 1)(|k_{zs}|^2 + k_\rho^2)(-|A_l^{TM}|^2) \\ +ik''_{zs}(e^{-2ik'_{zs}t_s} - 1)(|k_{zs}|^2 - k_\rho^2)(A_l^{TM} C_l^{TM^*}) \\ +ik''_{zs}(1 - e^{2ik'_{zs}t_s})(|k_{zs}|^2 - k_\rho^2)(A_l^{TM^*} C_l^{TM}) \\ +k'_{zs}(1 - e^{-2k''_{zs}t_s})(|k_{zs}|^2 + k_\rho^2)(-|C_l^{TM}|^2) \end{bmatrix} \tag{2.36}$$

$$g^{E}_{sl\theta\theta} g^{H^*}_{sl\rho\theta}\left(k_\rho, z_c = z_l, \omega\right) = \frac{ik_{zl}^*}{8k'_{zs}k''_{zs}|k_{zs}|^2} \times \begin{bmatrix} k'_{zs}(e^{2k''_{zs}t_s} - 1)(|A_l^{TE}|^2) \\ +ik''_{zs}(e^{-2ik'_{zs}t_s} - 1)(A_l^{TE} C_l^{TE^*}) \\ +ik''_{zs}(1 - e^{2ik'_{zs}t_s})(A_l^{TE^*} C_l^{TE}) \\ +k'_{zs}(1 - e^{-2k''_{zs}t_s})(-|C_l^{TE}|^2) \end{bmatrix} \tag{2.37}$$

Emitting Semi-Infinite Medium

Similarly, to the emitting thin film case, the integration over the semi-infinite volume has been performed analytically for the semi-infinite medium. The integration is performed with the following assumption with respect to z' of the Weyl components of the DGF [45]:

$$g^{E}_{sli\alpha}(k_\rho, z_c, z', \omega) g^{H^*}_{slj\alpha}(k_\rho, z_c, z', \omega) = g^{E}_{sli\alpha}(k_\rho, z_c, \omega) g^{H^*}_{slj\alpha}(k_\rho, z_c, \omega) e^{2k''_{zs} z'} \tag{2.38}$$

Then, the integration is calculated with the upper and lower limits of integration for the boundaries are: $z_{s+1} = 0$ and $z_s = -\infty$, respectively, resulting in the following expression:

$$q_{\omega,sl}(z_c = z_l) = \frac{k_v^2 \Theta(\omega, T_s)}{2\pi^2}$$

$$\times Re\left\{ i\varepsilon''_{rs}(\omega) \int_0^\infty \frac{k_\rho dk_\rho}{k''_{zs}} \begin{bmatrix} g^{E}_{sl\rho\rho}(k_\rho, z_c = z_l, \omega) g^{H^*}_{sl\theta\rho}(k_\rho, z_c = z_l, \omega) \\ + \; g^{E}_{sl\rho z}(k_\rho, z_c = z_l, \omega) g^{H^*}_{sl\theta z}(k_\rho, z_c = z_l, \omega) \\ - g^{E}_{sl\theta\theta}(k_\rho, z_c = z_l, \omega) g^{H^*}_{sl\rho\theta}(k_\rho, z_c = z_l, \omega) \end{bmatrix} \right\} \tag{2.39}$$

where the expression for each TM- and TE-polarized Weyl component is the following [45]:

$$g^{E}_{sl\rho\rho}(k_\rho, z_c = z_l, \omega) = \frac{ik_{zl}}{2k_s k_l}(A_l^{TM}) \tag{2.40}$$

$$g^{H}_{sl\theta\rho}(k_\rho, z_c = z_l, \omega) = \frac{k_l}{2k_s}(-A_l^{TM}) \tag{2.41}$$

$$g^{E}_{sl\rho z}(k_\rho, z_c = z_l, \omega) = \frac{ik_{zl}k_\rho}{2k_{zs}k_s k_l}(-A_l^{TM}) \tag{2.42}$$

$$g^{H}_{sl\theta z}(k_\rho, z_c = z_l, \omega) = \frac{k_l k_\rho}{2k_s k_{zs}}(A_l^{TM}) \tag{2.43}$$

$$g^{E}_{sl\theta\theta}(k_\rho, z_c = z_l, \omega) = \frac{i}{2k_{zs}}(A_l^{TE}) \tag{2.44}$$

$$g^{H}_{sl\rho\theta}(k_\rho, z_c = z_l, \omega) = \frac{k_{zl}}{2k_{zs}}(A_l^{TE}) \tag{2.45}$$

NFRHT formulation for anisotropic media

Based on equation (2.14) which expresses the electric and magnetic fields via the DGF and FDT, the NFRHT between anisotropic media is represented by the following expression [13,51,52]:

$$q = \frac{1}{8\pi^3}\int_0^\infty [\Theta(\omega,T_1) - \Theta(\omega,T_2)]d\omega \int_0^{2\pi}\int_0^\infty [\xi(\omega,k_\rho,\phi)\, k_\rho]dk_\rho d\phi \tag{2.46}$$

where ϕ is the azimuth angle corresponding to the angle of the plane of incidence. The term $\xi(\omega,k_\rho,\phi)$ is the energy transmission coefficient (ETC) or the phonon tunneling probability which can be expressed as [13]:

$$\xi(\omega,k_\rho,\phi) = \begin{cases} \mathrm{Tr}[(\mathbf{I}-\mathbf{R_2^*R_2}-\mathbf{T_2^*T_2})\mathbf{D}(\mathbf{I}-\mathbf{R_1^*R_1}-\mathbf{T_1^*T_1})\mathbf{D}^*], & \mathrm{k_\rho} < k_0 \\ \mathrm{Tr}[(\mathbf{R_2^*}-\mathbf{R_2})\mathbf{D}(\mathbf{R_1}-\mathbf{R_1^*})\mathbf{D}^*]e^{-2|k_{z2}''|d}, & \mathrm{k_\rho} > k_0 \end{cases} \tag{2.47}$$

The reflection and transmission coefficients are calculated at different values of the azimuth angle ϕ to cover a full rotation of the incident angle due to the anisotropy behavior of the material. Note that $\mathrm{Tr}(\cdot)$ represents the trace of a matrix and (*) represents the conjugate transpose. $\mathbf{I}$ is a 2 × 2 unit matrix and the matrix $\mathbf{D} = \left(\mathbf{I}-\mathbf{R_1R_2}e^{2ik_{z2}d}\right)^{-1}$. The reflection and transmission matrices are represented as:

$$\mathbf{R}_l = \begin{bmatrix} r_{ss}^l & r_{sp}^l \\ r_{ps}^l & r_{pp}^l \end{bmatrix}, \qquad \mathbf{T}_l = \begin{bmatrix} t_{ss}^l & t_{sp}^l \\ t_{ps}^l & t_{pp}^l \end{bmatrix}. \tag{2.48}$$

The first and second letters in the subscript of each coefficient indicate the polarization state of the incident wave and the reflected (or transmitted) wave, respectively. These coefficients can be obtained using the modified 4 × 4 transfer matrix method [13] or by their explicit expressions for each case [20,51,52]. The transmission matrix $\mathbf{T}_l = 0$ if the body has an optically large thickness to be considered a semi-infinite medium.

Chapter 3: NFRHT with Titanium Carbide MXene ($Ti_3C_2T_x$)

Introduction

NFRHT occurs when radiative heat transfer happens between objects separated by distances comparable to the characteristic thermal wavelength . In this regime, heat transfer magnitudes can surpass the blackbody limit due to additional energy transfer modes [46,53]. NFRHT has garnered significant interest lately due to its applications in various recent technologies, including sensing devices, nanoscale energy harvesting, and optoelectronic devices. An active research area on this field focuses on better controlling these heat flux magnitudes [12,14,23,25]. Researchers have suggested using new materials with unique optical properties to better manage these energy transfer modes. As a result, two-dimensional (2D) materials like graphene [19,21,24], black phosphorus (BP) [15,26], and hexagonal boron nitride (hBN) [12,54] have been extensively studied for their novel thermal and optical properties.

MXenes, a new family of 2D materials, comprising transition metal carbides, nitrides, or carbonitrides, have garnered significant attention since their discovery in 2011. Since the discovery of $Ti_3C_2T_x$ as the prototypical MXene, it has been the subject of extensive investigation, revealing a range of tunable optical properties, including emissivity, controllable bandgap [55–57], and surface plasmon (SP) resonances [58–60]. The exploration of the tunable SP resonance of $Ti_3C_2T_x$ MXene across a wide spectral range (from 2 to 6 μm) has highlighted its potential in manipulating the optical response within the mid-IR spectrum [61]. The tunability of SPs has made MXenes valuable for surface-enhanced Raman spectroscopy (SERS) [62], where thicker $Ti_3C_2T_x$ MXene films exhibit enhanced charge transfer effects and absorption in the NIR. Additionally, MXenes have showcased exceptional capabilities in thermal camouflage,

suitable for reducing radiation temperature through low mid-IR emissivity – attributes that contribute to multifunctionality, including discreet Joule heating and superior electromagnetic interference shielding efficiency [63,64].

The present study focuses on the NFRHT between Titanium Carbide MXene surfaces in a one-dimensional multi-layered structure. The complex dielectric function is the main property needed to fully characterize the optical behavior of the system. To this aim, samples were fabricated with various thicknesses of Titanium Carbide MXene on quartz substrates. The complex valued dielectric function of these samples was determined via spectroscopy ellipsometry, revealing a strong correlation between the radiative properties and the thickness of the MXene layers. The spectral and total net heat flux is calculated via DGF for FE where the scattering matrix method is employed to calculate the field amplitudes in each layer.

Theoretical Framework

The schematic for this work is presented in figure 8 and 9, where all the interfaces are assumed to be perfectly smooth surfaces. Each layer is described with its corresponding optical property represented by the complex-valued dielectric function $\varepsilon_l(\omega) = \varepsilon_l'(\omega) + i\varepsilon_l''(\omega)$.

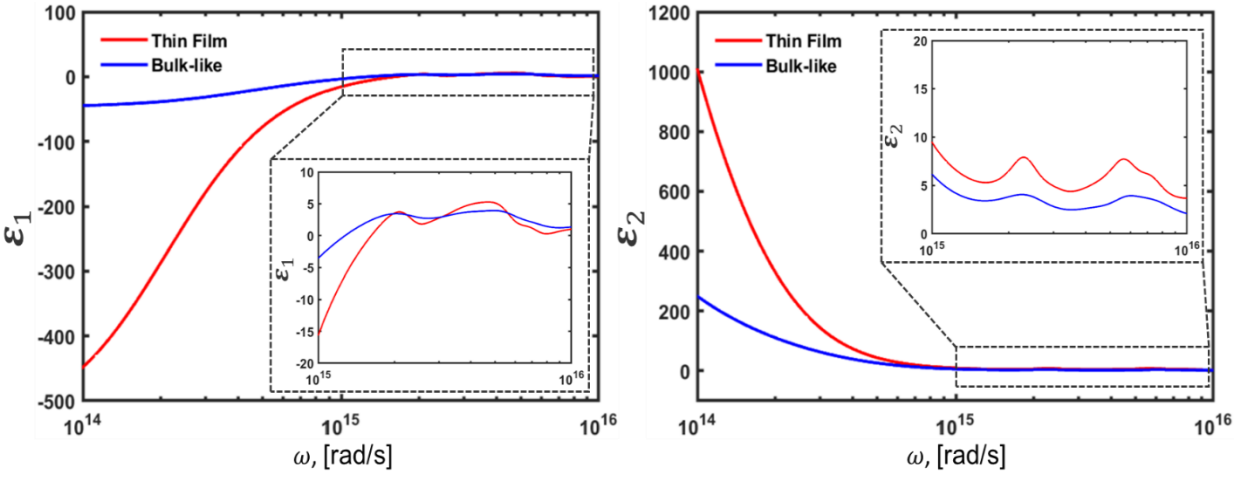

Figure 7: (a) Real and (b) imaginary part of the complex dielectric function of Titanium Carbide MXene.

The dielectric function for Silicon Carbide (SiC), Silicon Dioxide (SiO_2), Gold (Au), Copper (Cu), Platinum (Pt), Graphene and hexagonal Boron Nitride (hBN) can be found in the literature [13,22,65,66]. The dielectric function for MXene is presented in Figure 7 measured over thin films and bulk-like films.

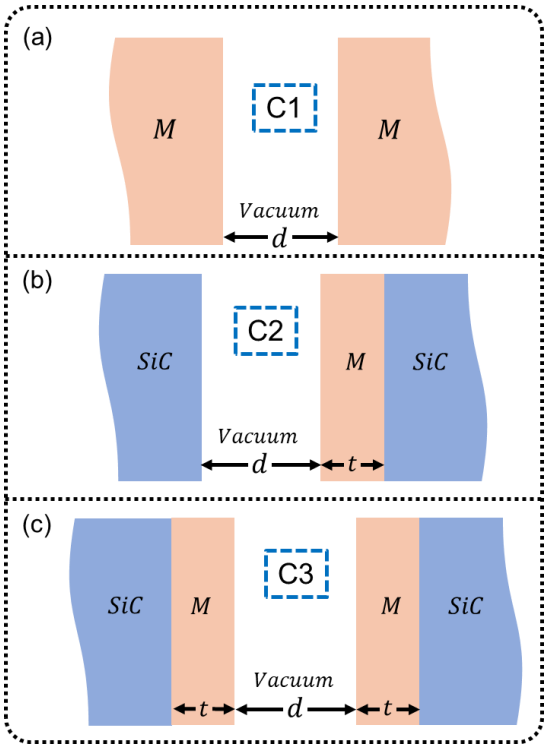

Figure 8: Schematic of the systems used for this work. (a) Case 1: Two semi-infinite media of the same material. (b) Case 2: Thin film of finite thickness t coated on a SiC slab. (c) Case 3: Thin film of finite thickness t coated on both SiC slabs. All separated by a vacuum gap distance d.

The first case (C1) evaluated will be a system of two semi-infinite media of the same material. The second (C2) and third case (C3) consists of a thin film of thickness t coated on a SiC slab. The NFRHT is calculated following FE theory were the Maxwell equations are augmented by a stochastic current density that accounts for the random fluctuations of charges due to thermal agitation. FDT links this stochastic current source term with the local temperature of the emitting body. The spectral radiative heat flux between these two bodies is calculated using the time average z-component of the Poynting vector and by then applying the FDT where the DGF are calculated for a specific geometry and boundary conditions [10,47]:

$$q_{\omega}^{prop} = \frac{[\Theta(\omega, T_1) - \Theta(\omega, T_3)]}{4\pi^2} \int_0^{k_0} k_\rho \cdot \boldsymbol{Z}_{13}^{prop} dk_\rho \tag{3.1}$$

$$q_{\omega}^{evan} = \frac{[\Theta(\omega, T_1) - \Theta(\omega, T_3)]}{\pi^2} \int_{k_0}^{k_\infty} k_\rho \cdot \boldsymbol{Z}_{13}^{evan} \cdot e^{-2k_{z2}'' d} dk_\rho \tag{3.2}$$

Where the total heat flux is the sum of the contributions of the propagating evanescent waves, i. e. $q_{\omega,C} = q_{\omega,C}^{prop} + q_{\omega,C}^{evan}$. The corresponding energy transmission coefficients ($\boldsymbol{Z}_{ij}^{prop,evan}$) are expressed as:

$$\boldsymbol{Z}_{13,C3}^{prop} = \sum_{\gamma=TE,TM} \frac{(1 - |R_1^\gamma|^2 - |T_1^\gamma|^2)(1 - |R_3^\gamma|^2 - |T_3^\gamma|^2)}{|1 - R_1^\gamma R_3^\gamma \mathrm{e}^{2ik_{z2}d}|^2} \tag{3.3}$$

$$\boldsymbol{Z}_{13.C3}^{evan} = \sum_{\gamma=TE,TM} \frac{\mathrm{Im}(R_1^\gamma)\mathrm{Im}(R_3^\gamma)}{|1 - R_1^\gamma R_3^\gamma \mathrm{e}^{2ik_{z2}d}|^2} \tag{3.4}$$

Where R_l^γ and T_l^γ represent the reflection and transmission coefficients with polarization state γ, respectively. The expressions for these coefficients are as follows:

$$R_l^\gamma = \frac{r_{l-1,l}^\gamma + r_{l,l+1}^\gamma \mathrm{e}^{2ik_{zl}t_l}}{1 + r_{l-1,l}^\gamma r_{l,l+1}^\gamma \mathrm{e}^{2ik_{zl}t_l}} \tag{3.5}$$

$$T_l^\gamma = \frac{t_{l-1,l}^\gamma t_{l,l+1}^\gamma \mathrm{e}^{ik_{zl}t_l}}{1 + r_{l-1,l}^\gamma r_{l,l+1}^\gamma \mathrm{e}^{2ik_{zl}t_l}} \tag{3.6}$$

where r_{ij}^γ and t_{ij}^γ are the Fresnel reflection and transmission coefficients of the interface between layer i and j, respectively. These coefficients are represented by:

$$r_{ij}^{TE} = \frac{k_{iz} - k_{jz}}{k_{iz} + k_{jz}} \tag{3.7}$$

$$r_{ij}^{TM} = \frac{\varepsilon_j k_{iz} - \varepsilon_i k_{jz}}{\varepsilon_j k_{iz} + \varepsilon_i k_{jz}} \tag{3.8}$$

$$t_{ij}^{TE} = \frac{2k_{iz}}{k_{iz} + k_{jz}} \tag{3.9}$$

$$t_{ij}^{TM} = \frac{2\varepsilon_j k_{iz}}{\varepsilon_j k_{iz} + \varepsilon_i k_{jz}} \sqrt{\frac{\varepsilon_i}{\varepsilon_j}} \tag{3.10}$$

Note: Equations (3.3-4) represent the exchange functions for semi-infinite medium coated with a thin film, as represented in case C3. For the case of only semi-infinite medium, like case C1, $t_l \to \infty$. This will cause the exponential term ($e^{ik_{zl}t_l}$), drop to zero as $t_l \to \infty$. Therefore, $T_l^{\gamma} \to 0$, while $R_l^{\gamma} \to r_{l-1,l}^{\gamma}$ which will then match what is reported in literature for the energy transmission coefficients for NFRHT between two semi-infinite media:

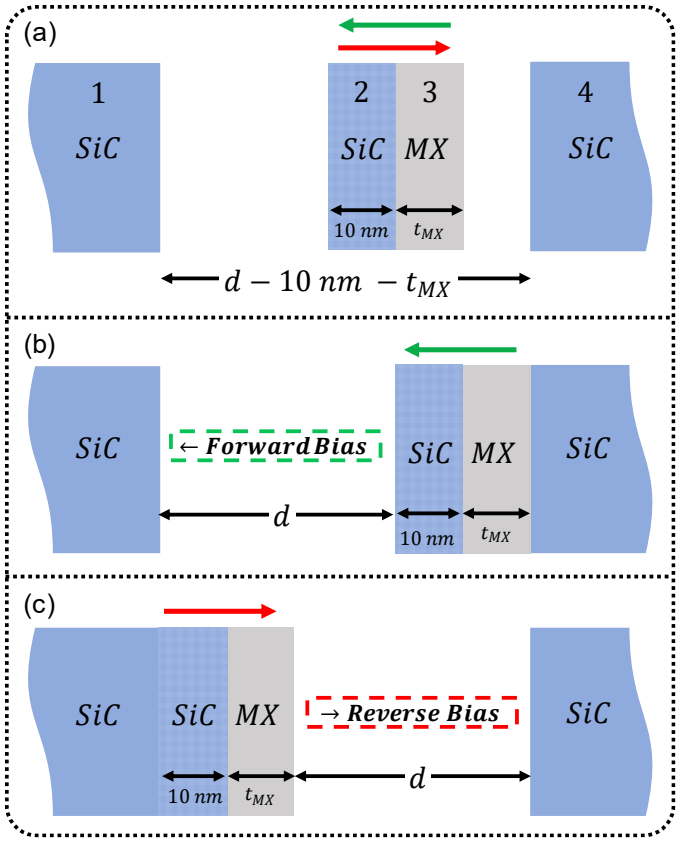

Figure 9: (a) Rectification case using a movable medium body made two thin films of MXene and SiC Representation the forward bias (a) where one of the SiC slabs is coated by a double film of MXene and SiC and the reverse bias (c) where one of the SiC can be assumed to only be coated by a MXene film.

$$\boldsymbol{Z}_{13,C1}^{prop} = \sum_{\gamma=TE,TM} \frac{(1-\left|r_{21}^{\gamma}\right|^2)(1-\left|r_{23}^{\gamma}\right|^2)}{|1-r_{21}^{\gamma}r_{23}^{\gamma}e^{2ik_{z2}d}|^2} \tag{3.11}$$

$$\boldsymbol{Z}_{13,C1}^{evan} = \sum_{\gamma=TE,TM} \frac{\mathrm{Im}(r_{21}^{\gamma})\mathrm{Im}(r_{23}^{\gamma})}{|1-r_{21}^{\gamma}r_{23}^{\gamma}e^{2ik_{z2}d}|^2} \tag{3.12}$$

Case C2 will use the transmission coefficients representation from equations (3.3-4) for the thin film coated SiC slab and equations (3.11-12) for the SiC slab.

The proposed rectification concept is illustrated in Figure 9(a) where the system consists of two semi-infinite media fixed at the ends of the system. The middle movable layer consists of a double film of MXene, and Sic. The middle layer is assumed to make full contact with one of the fixed SiC slabs transforming it into a fully new medium. When moving the middle layer and attaching it to the right side, the system will by a bare SiC slab and a multilayer coated SiC slab separated by a vacuum gap. This first configuration creates a multilayer structure where the SiC slab and the SiC thin film share similar resonant modes causing a higher magnitude of NFRHT. Thus, this will be considered as the forward bias. When the middle layer is attached to the left side, the system will be a bare SiC slab and a coated SiC slab with a thin film of MXene. This configuration brings an asymmetry on the resonance modes of the materials, causing a lower magnitude of NFRHT. The rectification effect is then achieved by creating an on- and off-resonance with the modes of the SiC slab. It is crucial to acknowledge that although the configuration proposed by the theoretical model may be challenging to achieve with current nanofabrication techniques, the insights from the proposed mechanism can better showcase capabilities of this new material.

The performance of the system will be quantified by a rectification percentage:

$$R[\%] = \frac{q_f - q_r}{q_f} \times 100\% = 1 - \frac{q_r}{q_f} \times 100\% \tag{3.13}$$

where q_f and q_r are the forward and reverse bias neat heat fluxes, respectively. These magnitudes of heat flux are calculated using the 1D layered media using DGF and S-matrix [45]. For all the cases, the emitting body will be considered as the one attached with the middle layer, therefore, the emitting body for the forward bias is the multilayered coated SiC slab and the emitting body for the reverse bias is the coated SiC slab with a thin film of MXene. The net heat flux towards the SiC slab for the forward bias can be expressed as the sum of the contributions of each layer [22,67], i. e., $q_f = q_{4\to1} + q_{3\to1} + q_{2\to1} = q_{432\to1}$, and similarly for the reverse bias, $q_r = q_{12\to4} + q_{3\to4} = q_{123\to4}$ following the numbering scheme described in Figure 9(a). The contribution for the SiC slab and thin film will be considered as a single SiC slab.

The calculations for the spectral heat flux $q_{\omega,3\to1}$, $q_{\omega,2\to1}$, and $q_{\omega,3\to4}$ are performed using the spectral heat flux due to an emitting thin film along the z-direction:

$$q_{\omega,film}(z_l) = \frac{k_0^2[\Theta(\omega,T_s) - \Theta(\omega,T_l)]}{\pi^2}$$
$$\times Re\left\{ i\varepsilon_s''(\omega) \int_0^\infty k_\rho dk_\rho \int_0^{t_s} dz' \begin{bmatrix} g_{sl\rho\rho}^E(k_\rho, z_l, z', \omega) g_{sl\theta\rho}^{H^*}(k_\rho, z_l, z', \omega) \\ +g_{sl\rho z}^E(k_\rho, z_l, z', \omega) g_{sl\theta z}^{H^*}(k_\rho, z_l, z', \omega) \\ -g_{sl\theta\theta}^E(k_\rho, z_l, z', \omega) g_{sl\rho\theta}^{H^*}(k_\rho, z_l, z', \omega) \end{bmatrix} \right\} \tag{3.14}$$

where $q_{\omega,film}(z_l)$ represents the spectral heat flux calculated at layer l, and t_s is the thickness of the emitting source layer. Consequently, the calculations for the spectral heat flux $q_{\omega,4\to1}$ and $q_{\omega,12\to4}$ are performed using the spectral heat flux due to an emitting semi-infinite along the z-direction:

$$q_{\omega,bulk}(z_l) = \frac{k_0^2[\Theta(\omega,T_s) - \Theta(\omega,T_l)]}{2\pi^2}$$

$$\times Re\left\{ i\varepsilon_s''(\omega) \int_0^\infty \frac{k_\rho dk_\rho}{k_{zs}''} \begin{bmatrix} g_{sl\rho\rho}^E(k_\rho,z_l,\omega) g_{sl\theta\rho}^{H^*}(k_\rho,z_l,\omega) \\ + \; g_{sl\rho z}^E(k_\rho,z_l,\omega) g_{sl\theta z}^{H^*}(k_\rho,z_l,\omega) \\ -g_{sl\theta\theta}^E(k_\rho,z_l,\omega) g_{sl\rho\theta}^{H^*}(k_\rho,z_l,\omega) \end{bmatrix} \right\} \quad (3.15)$$

where $q_{\omega,bulk}(z_l)$ represents the spectral heat flux calculated at layer l.

T_s and T_l represent the temperatures of the source and receiving layer, respectively. The temperature of the middle layer will be fixed to be the higher temperature. This means that the SiC slab attached to the middle layer will have the same temperature, while the SiC slab at the other end has the lower temperature.

Results and Discussion

For the case C1, both surfaces are assumed to be semi-infinite, with their respective temperatures to be $T_1 = 300\ K$ and $T_3 = 370\ K$. The net radiative heat flux for this is reported in Figure 10, as function of gap distances d. The plot incorporates the cases for dielectrics and metallic surfaces for better comparison. As seen in Figure 10, the behavior of $Ti_3C_2T_x$ MXene falls in between the magnitudes of the other metallic surfaces. Even though, this material is well known for its metallic-dielectric transition on its optical properties, the trend resembles the features of metallic surfaces, which are different from the dielectrics as that linear increase of heat flux with respect to gap distance is attributed to the bulk SPhPs which are not present in a metallic material, like $Ti_3C_2T_x$ MXene []. At gap distances far from 100 nm, the magnitudes of heat flux tend to be above the magnitudes of the other metals used in this study. At gap distances lower than 100 nm, the metallic surfaces, including $Ti_3C_2T_x$ MXene, show a weaker relation to the gap distance. As mentioned in Ref. [66], the saturation of the heat flux with respect to gap distance for the

metallic cases has close relation to the energy transmission coefficient for evanescent TE modes ($\boldsymbol{Z}_{13}^{prop,\mathrm{TE}}$), where this coefficient depends on the wavevector in vacuum (k), as shown in equation (3.16):

$$\boldsymbol{Z}_{13}^{prop,\mathrm{TE}} \propto \{\mathrm{Im}[r_{i2}^{TE}]e^{-kd}\}^2 \tag{3.16}$$

where r_{i2}^{TE} is the Fresnel reflection coefficient for TE waves in the vacuum and layer i interface. It can be seen from this equation (3.16) that the energy transfer coefficient will decrease as the gap distance decreases, knowing that $\mathrm{Im}[r_{i2}^{TE}]$ does not increase with increasing wavevector (k). It has been shown that there is a cutoff wavevector $k_{cutoff} \approx \omega_p/c_0$, having ω_p as the plasmonic frequency of the material, where the . $d_{critical} = 1/k_{cutoff} = c_0/\omega_p$ where for semi-infinite $Ti_3C_2T_x$ MXene slabs $d_{critical} \approx$ 160 nm, where for Au is 30 nm and for Pt is 17.8 nm. This can be clearly seen in Figure 10 as why the values of $Ti_3C_2T_x$ MXene has an earlier plateau trend compared to the other metals.

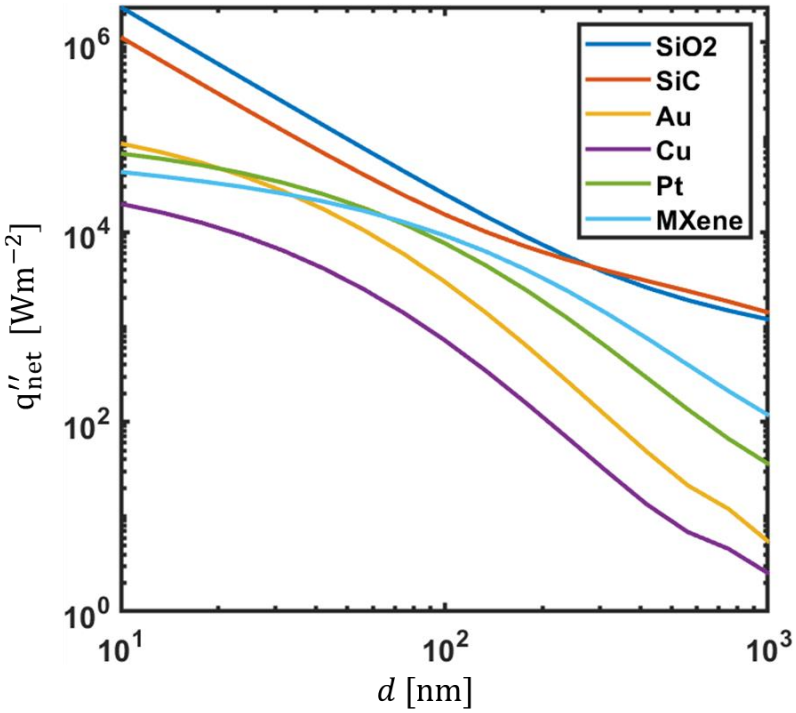

Figure 10: Net heat flux as a function of gap distance for two similar semi-infinite media using dielectrics and metallic surfaces.

For case C2 (represented in Figure 7b), the same temperature biased from the previous case is used here. The material $\boldsymbol{M}$ for the coated films is $Ti_3C_2T_x$ MXene and other 2D materials, hBN and Graphene, for better comparison. Figure 11 shows the net radiative heat flux as a function of gap distance d for the three cases using a coated thin film of thickness $t = 10\ nm$. For the case of a coated SiC slab, the magnitudes of heat flux for the case using hBN dominate over using $Ti_3C_2T_x$ MXene are Graphene. The SPhPs for hBN and SiC have a better coupling which causes higher magnitudes even with an asymmetry on the structure. For the case of two coated SiC slabs, the magnitudes of heat flux are higher for the case using $Ti_3C_2T_x$ MXene and hBN thin films. The high magnitudes using hBN thin films are due to the hyperbolic phonon polaritons (HSPhPs) resonance that are within the mid-IR range along with the SPhPs of SiC [12,15,68].

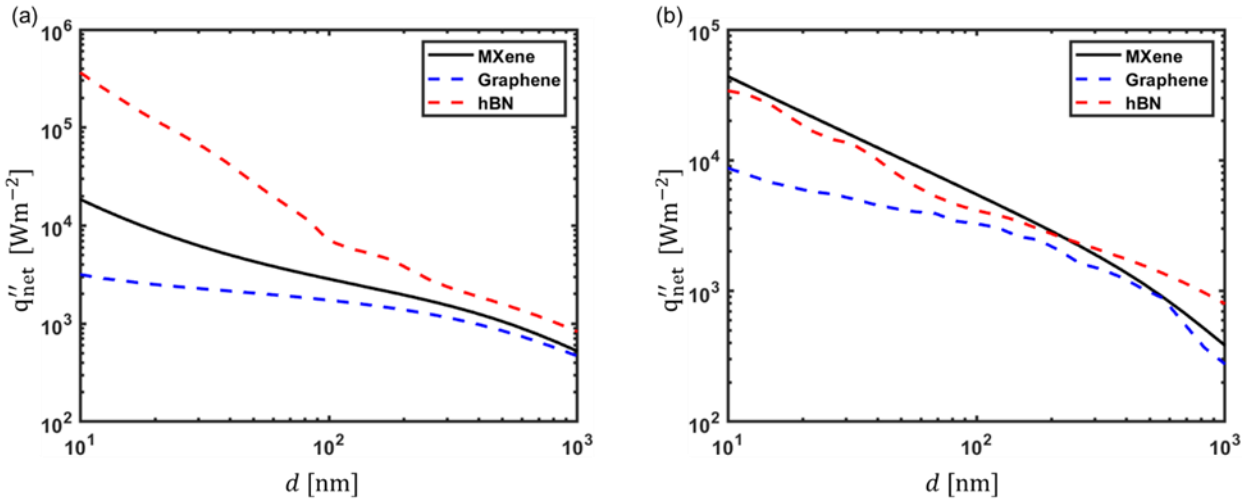

Figure 11: Net heat flux as a function of gap distance for (a) a SiC slab and a coated SiC and (b) for two coated SiC slabs. The coatings used have a thickness of 10 nm.

For the rectification case, the forward bias and reverse bias are represented in Figure 12 (solid lines and dashed lines, respectively). The forward bias shows and increment on the values of heat flux below the 200 nm gap distances which can be represented by the coupling of the SPhPs of the thin film. This resonance not only happens at one of the interfaces of the material but at both

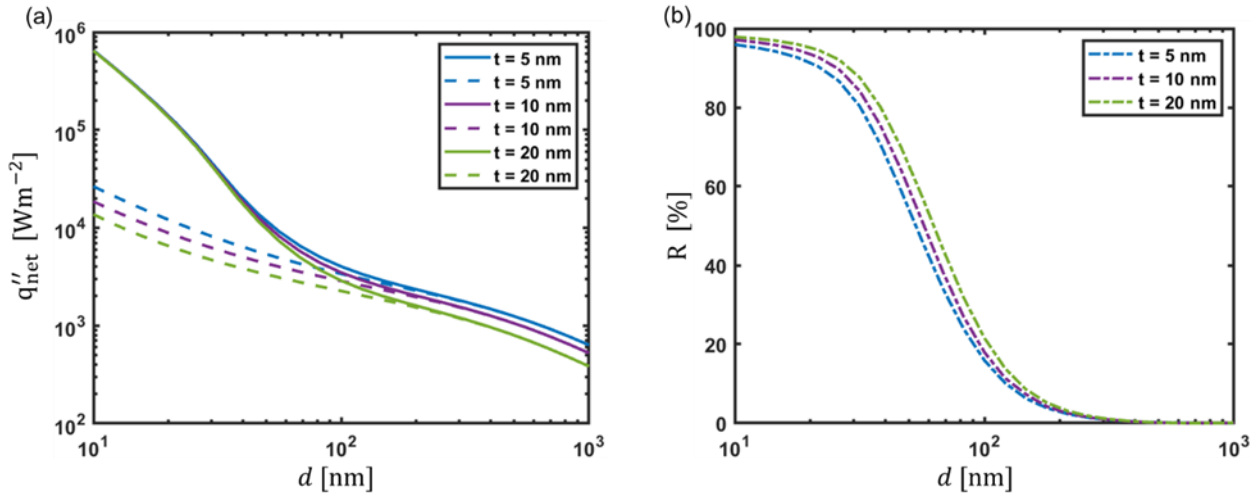

Figure 12: (a) Net heat flux as a function of gap distance for the forward bias (solid lines) and reverse bias (dashed lines) at different $Ti_3C_2T_x$ MXene thin film thickness. (b) Rectification percentage as a function of gap distance for the different thicknesses.

of the interfaces. Meaning that at smaller gaps, the SiC slab can sense the SPhPs of the interface between the SiC thin film and the $Ti_3C_2T_x$ MXene. Also, it is seen from the forward case that for gap distances bellow 40 nm, the magnitudes of heat flux are not dependent on thickness due to the fact that the phonon interaction between the SiC slab and SiC thin film that dominate over the presence of a metallic thin film. For the reverse scenario, for gap distance below 200 nm shows that the $Ti_3C_2T_x$ MXene film continues to break the symmetry within the phononic resonances of the system. Despite the asymmetry, the magnitude of heat flux continues to increase in the reverse bias as an effect of the SiC slabs surface modes are able to get through the $Ti_3C_2T_x$ MXene thin film. As a result, the magnitudes of rectification are above 80% at gap distance bellow 200 nm.

Conclusion

In summary, the impact of $Ti_3C_2T_x$ MXene in NFRHT for semi-infinite and thin film media have been investigated. For the case of semi-infinite slabs of $Ti_3C_2T_x$ MXene, the magnitudes of heat flux report a trend similar to other metallic surfaces. The magnitudes start to plateau at $d_{critical} \approx$ 160 nm which is larger in comparison to other metals. In the case of $Ti_3C_2T_x$ MXene thin films, the magnitudes are within the magnitude of hBN and Graphene thin films. The coupling between $Ti_3C_2T_x$ MXene and the SPhP of SiC is not as strong as it is for the hBN thin film case where HSPhPs modes are also present. The rectification case was evaluated using a system with a moveable film of SiC and $Ti_3C_2T_x$ MXene films which causes and on- and off-resonance coupling between the SiC slabs. The forward bias at smaller gap distances shows an increase in magnitudes of heat flux with respect to gap distance independent of the $Ti_3C_2T_x$ MXene film thickness. As for the reverse bias, the $Ti_3C_2T_x$ MXene film controlled the magnitudes of heat flux from the SiC slabs by breaking the symmetry in the resonant modes. This work shows the capabilities that $Ti_3C_2T_x$ MXene can be used for NFRHT in order to manipulate the magnitudes of heat flux compared to other 2D materials and metallic surfaces.

Chapter 4: NFRHT with Cobalt Slanted Columnar Thin Films

Introduction

Surface roughness, patterning, and nanostructures have been employed to precisely adjust radiative responses, particularly spectral and directional properties. Advances in microfabrication and enhanced computing capabilities have enabled more systematic studies on how microstructures and material properties influence thermal emission and absorption characteristics [29,30]. Glancing angle deposition (GLAD) is a promising nanofabrication technique that produces spatially coherent, highly porous, super lattice-type three-dimensional nanomorphologies [69,70]. This bottom-up physical vapor deposition technique uses particle flux at an oblique angle of incidence along with a precise sample manipulator, allowing for the fabrication of versatile 3D nanostructures on a wafer-scale substrate [70,71]. Generalized ellipsometry, a highly effective non-invasive optical technique, is used to determine the anisotropic optical properties of complex nanostructured thin films and to extract structural parameters through best-match model analysis [72–74].

Sculptured thin films via GLAD exhibit unique properties that can potentially make them highly effective for manipulating NFRHT. Slanted columnar thin films, angled relative to the substrate, create a birefringent medium. This anisotropy enables the control of the polarization and propagation direction of electromagnetic waves. The structural design allows for the excitation of tailored resonant modes [75–77]. These resonances can be engineered by adjusting the angle, height, and periodicity of the columns [78]. The unique properties of anisotropic metasurfaces fabricated via GLAD are critical for advancing technologies that rely on NFRHT. The ability to control the direction, polarization, and resonant modes of thermal radiation enhances the

efficiency and performance of TPV systems by optimizing the emission spectra to match photovoltaic cell characteristics [79,80]. In thermal management, these metasurfaces can be used to facilitate efficient heat dissipation and localized heating or cooling, addressing critical challenges in electronic device reliability.

This study numerically investigates the NFRHT between two slanted columnar thin films made of cobalt separated by a vacuum gap. The NFRHF is calculated at different gap distances. Also, the modulation of NFRHF by controlling the relative rotation angle between the receiver and the emitter is investigated. The calculations performed in this study are based on the fluctuation-dissipation theorem combined with the modified 4×4 transfer matrix method. By adopting the enhanced matrix approach, this method is capable of calculating the NFRHT between two homogeneous media well as stratified media efficiently while avoiding the problem of numerical overflow when dealing with evanescent waves [13].

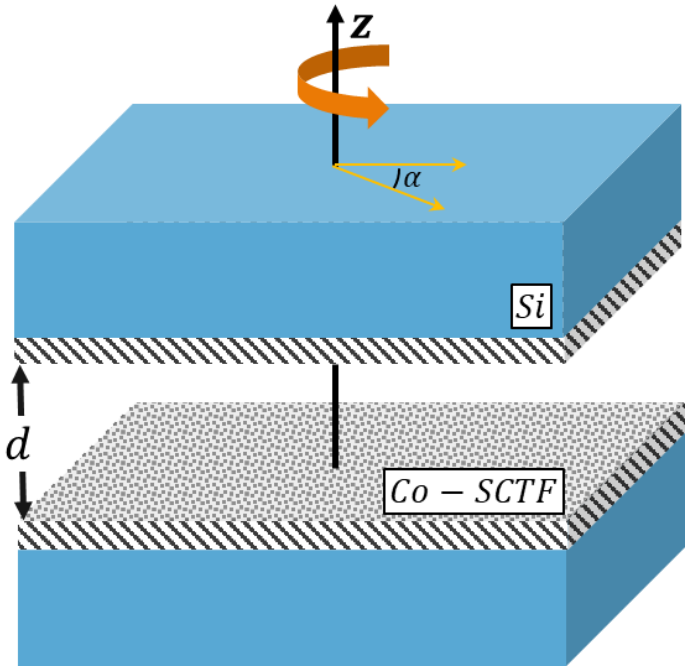

Figure 13: Schematic of NFRHT between two Co-SCTF. The rotation angle (α) is measured along the z-axis.

Theoretical Framework

The numerical analysis of the NFRHT with Co-SCTF is performed with two parallel surfaces with the nanostructures facing each other at a gap distance d, represented by figure 10. The Co-SCTF were growth on a Silicon substrate. Therefore, the structure considered for this study is a semi-infinite medium coated with a thin film. The structural parameters, like column slanting angle (θ_s) and thin film thickness (t), along with the wavelength dependent dielectric function

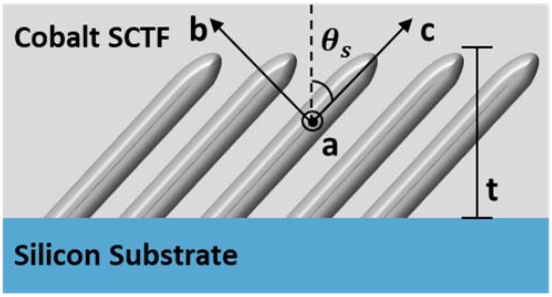

Figure 14: Representation of the polarizability coordinates for Co-SCTF.

were determined by a homogeneous biaxial layer approach (HBLA) physical model incorporating the data gathered experimentally via generalized spectroscopy ellipsometry [81].

The complex-value dielectric tensor of the Co-SCTF is expressed in terms of the three major cartesian dielectric polarizability axes represented by (a, b, c) coordinates forming an orthorhombic system [42]:

$$\varepsilon = \begin{bmatrix} \varepsilon_a & 0 & 0 \\ 0 & \varepsilon_b & 0 \\ 0 & 0 & \varepsilon_c \end{bmatrix} \tag{4.1}$$

A transformation from the polarizability axes to the cartesian coordinates is needed for the mathematical model used in this work. The rotation matrix $\boldsymbol{B}$ represents the coordinate transformation from $(a,\ b,\ c)$ coordinates to the $(x,\ y,\ z)$ coordinates [48,82]:

$$\boldsymbol{B} = \begin{bmatrix} \cos\phi_E \cos\psi_E - \sin\phi_E \cos\theta_E \sin\psi_E & -\cos\phi_E \sin\psi_E - \sin\phi_E \cos\theta_E \cos\psi_E & \sin\phi_E \sin\theta_E \\ \sin\phi_E \cos\psi_E + \cos\phi_E \cos\theta_E \sin\psi_E & -\sin\phi_E \sin\psi_E - \cos\phi_E \cos\theta_E \cos\psi_E & -\cos\phi_E \sin\theta_E \\ \sin\theta_E \sin\psi_E & \sin\theta_E \cos\psi_E & \cos\theta_E \end{bmatrix} \quad (4.2)$$

where $(\phi_E,\ \theta_E,\ \psi_E)$ are the Euler angles. The transformation from $(a,\ b,\ c)$ coordinates to the $(x,\ y,\ z)$ coordinates can represented as:

$$\begin{bmatrix} \varepsilon_{xx} & \varepsilon_{xy} & \varepsilon_{xz} \\ \varepsilon_{yx} & \varepsilon_{yy} & \varepsilon_{yz} \\ \varepsilon_{zx} & \varepsilon_{zy} & \varepsilon_{zz} \end{bmatrix} = \boldsymbol{B} \begin{bmatrix} \varepsilon_a & 0 & 0 \\ 0 & \varepsilon_b & 0 \\ 0 & 0 & \varepsilon_c \end{bmatrix} \boldsymbol{B}^T \quad (4.3)$$

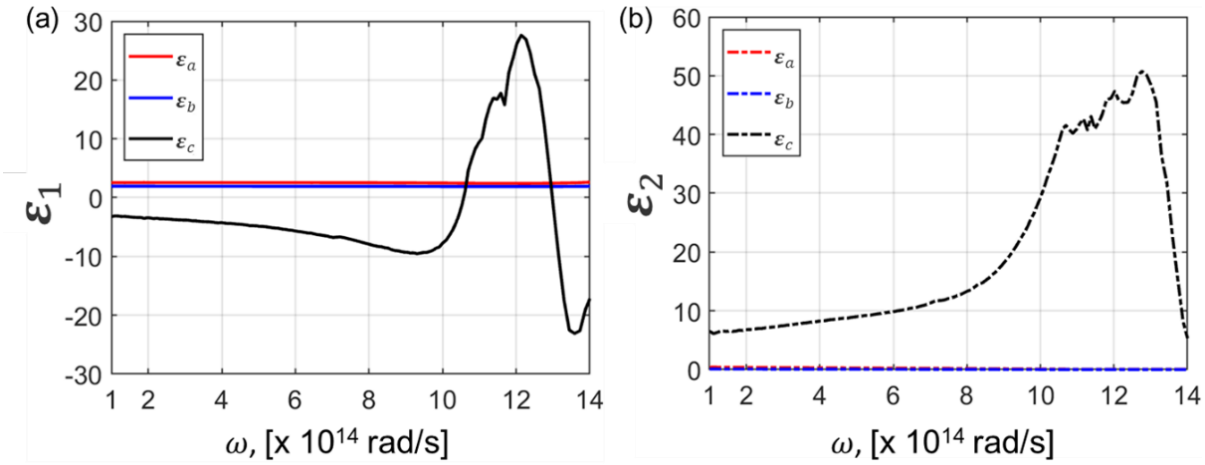

Figure 15: Complex-valued dielectric function for the Co-SCTF determined by spectroscopic ellipsometry via HBLA showing the (a) real and (b) imaginary part.

Based on the electric and magnetic fields via the DGF and FDT, the NFRHT between anisotropic media is represented by the following expression [13,51,52]:

$$q = \frac{1}{8\pi^3}\int_0^\infty [\Theta(\omega, T_1) - \Theta(\omega, T_3)]d\omega \int_0^{2\pi}\int_0^\infty [\xi(\omega, k_\rho, \phi)\cdot k_\rho]dk_\rho d\phi \quad (4.4)$$

where ϕ is the azimuth angle and $\xi(\omega, k_\rho, \phi)$ is the energy transmission coefficient (ETC) or the phonon tunneling probability which can be expressed as [13]:

$$\xi(\omega, k_\rho, \phi) = \begin{cases} \mathrm{Tr}[(\mathbf{I} - \mathbf{R_3^*R_3} - \mathbf{T_3^*T_3})\mathbf{D}(\mathbf{I} - \mathbf{R_1^*R_1} - \mathbf{T_1^*T_1})\mathbf{D}^*], & \mathrm{k_\rho} < k_0 \\ \mathrm{Tr}[(\mathbf{R_3^*} - \mathbf{R_3})\mathbf{D}(\mathbf{R_1} - \mathbf{R_1^*})\mathbf{D}^* e^{-2|k_{z2}''|d}, & \mathrm{k_\rho} > k_0 \end{cases} \quad (4.5)$$

I is a 2 × 2 unit matrix and the matrix $\mathbf{D} = \left(\mathbf{I} - \mathbf{R_1}\mathbf{R_2}e^{2ik_{z2}d}\right)^{-1}$. The reflection and transmission matrices are represented as:

$$\mathbf{R}_l = \begin{bmatrix} r_{ss}^l & r_{sp}^l \\ r_{ps}^l & r_{pp}^l \end{bmatrix}, \qquad \mathbf{T}_l = \begin{bmatrix} t_{ss}^l & t_{sp}^l \\ t_{ps}^l & t_{pp}^l \end{bmatrix}. \tag{4.6}$$

These coefficients are obtained using the modified 4 × 4 transfer matrix method [13] but they could also be obtained by their explicit expressions for each case [20,51,52]. The transmission matrix $\mathbf{T}_l = 0$ if the body has an optically large thickness to be considered a semi-infinite medium.

Results and Discussion

In this study, the temperature of the two bodies is set at $T_1 = 370$ K and $T_3 = 300\ K$. The structure parameters of the Co-SCTF extracted via HBLA are the slanting angle of the columnar structure $\theta_s = 59°$ and thickness (height) of the sculptured film $t = 235\ nm$. The NFRHF is calculated in terms of the gap distance d and rotation angle α around the z-direction which is the propagation direction of radiative heat transfer. Only one of the bodies is rotated while the other remains in a fixed position. The cases shown in Figure 16 are for 10 nm, 100 nm, and 1000 nm gap distance with respect to the rotation angle. As seen in the case with the larger gap distance, the magnitudes of heat flux across the system tend to show a periodic trend where the maximum is established at 0 degrees and a minimum at 180 degrees meaning that there is a better matching within the two bodies when the nanostructures are aligned compared to when they are misaligned. As the gap distance decreases, as seen in the case of 100 nm, the values for the minimum heat flux tend to shift from 180 degrees to values between 90 and 135 degrees. Along with this behavior, there is a new peak of heat flux happening at 180 degrees. This shows that

now that other than the alignment within the structures like how it is happening at 0 degrees, the nanostructures can sense the fields localized at the tip of the nanostructures. These fields could be caused by induced dipole moments that are normally seen in this type of structure. The slanted columnar structures introduce anisotropy, which affects how electric fields interact with the material. When an electromagnetic wave impinges on the nanostructure, the slanted columns induce dipole moments that are directionally dependent [83]. These induced dipoles can resonate at specific frequencies, significantly enhancing the local electromagnetic fields. This effect is seen in the case where the gap distance is 10 nm, seen in Figure 16. At this distance, the structure effects are stronger due to the similarity of sizes between the geometrical features and the relative distance between the surfaces. Figure 17 shows the periodical behavior of the normalized net heat flux within this Co-SCTF as a function of gap distance. The trend tends to drastically change within the 10 nm to 100 nm range as the induced fields from the nanostructures of both bodies better interact with each other. It is also interesting to notice that below the 100 nm range, the point where the minimum heat flux was due to misalignment of the nanostructures, transitions into another maximum point.

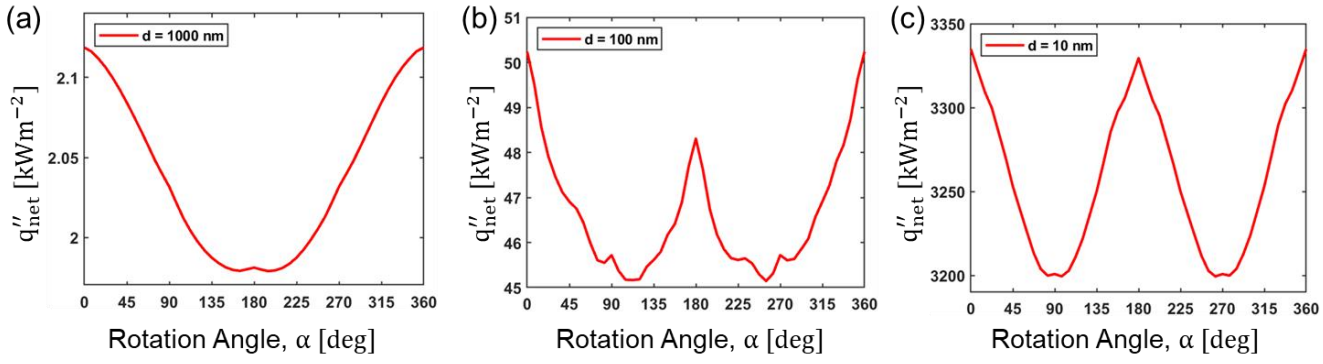

Figure 16: Net heat flux between Co-SCTF at 10 nm, 100 nm, and 1000 nm of vacuum gap distance.

At distances between 10 nm to 100 nm, the net heat flux already exceeds what is normally expected for metallic surfaces, as seen in Figure 18. The enhancement of the magnitudes of heat flux can be case of enhanced electromagnetic field confinement [78,84–86]. The unique morphology of these structures enhances the confinement of electromagnetic fields at the surfaces, increasing the local density of states. As the gap distance decreases, this enhancement increases as there is a better coupling between the resonances of the structural features.

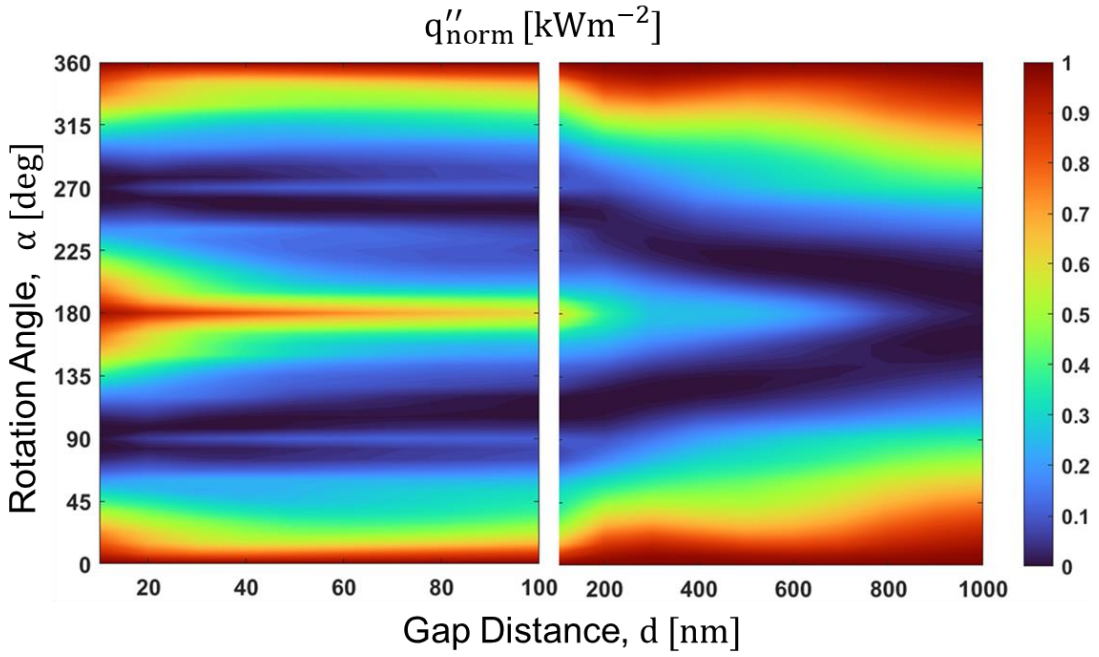

Figure 17: Contour map of normalized heat flux as a function of rotation angle α and a gap distance d.

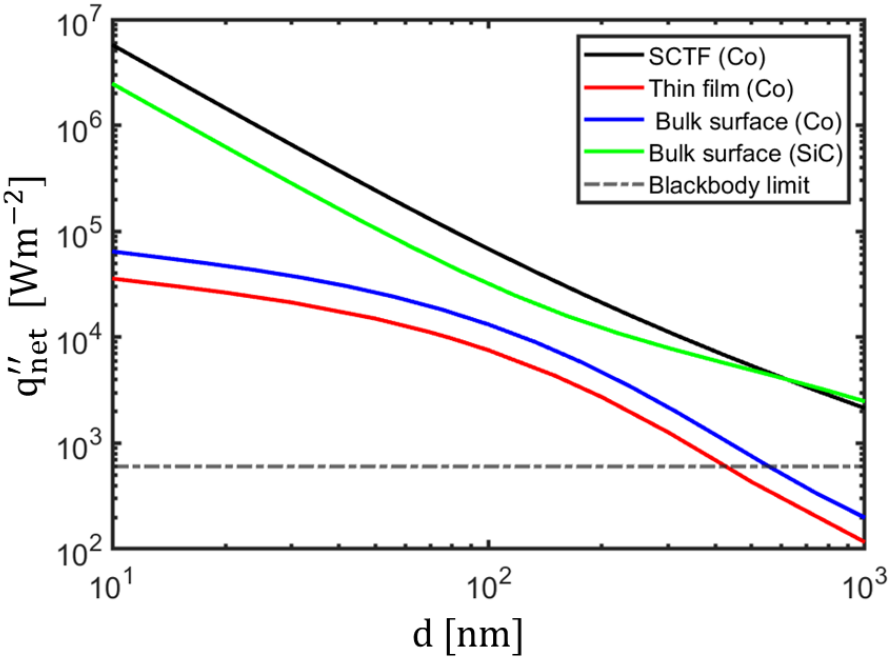

Figure 18: Net heat flux as a function of gap distance for the Co-SCTF in comparison with Co thin films (red) and bulk surfaces (blue) as well as SiC surfaces (green). The horizontal dashed line represents the blackbody limit.

Conclusion

The effects of NFRHT using slanted columnar thin films made of Cobal were investigated as well as the effects on orientation of the nanostructures and gap distance between the surfaces. The results show a periodical trend as a function of gap distance. At large gap distances $d > 100\ nm$, the maximum and minimum net heat flux is achieved when both surfaces are aligned and misaligned (by 180 degrees), respectively However, for gap distances between $10\ nm < d < 100\ nm$, the trend changes causing a transition of the minimum heat location at 180 degrees to be a maximum at closer gap distances. Overall, the magnitudes of heat flux are higher compared to bare slabs and thin films of Cobalt showing an enhancement due to the tailoring of the optical properties due to the nanostructures. The results obtained in this study may provide better understanding of the capabilities of slanted columnar thin films in modulating NFRHT between anisotropic surfaces.

Summary and Outlook

This thesis explores advanced mechanisms for manipulating Near-Field Radiative Heat Transfer (NFRHT) using two-dimensional materials and nanostructured surfaces. The focus of the study is on understanding how these materials and structures can better manipulate the magnitudes of radiative heat transfer in the nanoscale regime. The research is divided into two main parts, each addressing a different material system: Titanium Carbide MXene and Cobalt Slanted Columnar Thin Films (Co-SCTF).

In the first part of the thesis, the radiative thermal transport properties of Titanium Carbide MXene are investigated. For this study, Titanium Carbide MXene samples of varying thicknesses were fabricated using a layer-by-layer spin-coating technique on quartz substrates. Spectroscopic ellipsometry was performed over a broad spectral range, from mid-infrared to vacuum ultraviolet, to determine radiative properties of the MXene layers.

The findings revealed that the thickness of the MXene layers significantly influences their radiative properties. Calculations of the spectral and total radiative heat flux between these samples in the near-field regime showed that MXenes could play a superior role in controlling radiative heat transfer compared to traditional materials. The ability to manipulate NFRHT using MXenes opens up possibilities for enhanced thermal management in electronic devices and other applications where efficient heat dissipation is crucial.

In the case presented in this thesis, the characterization of its radiative properties was conducted using a colloidal solution of nanosized flakes. However, there is potential for more precise characterization. Future studies should perform optical characterization on individual flakes of this 2D material to gain a deeper understanding of its properties based on the number of

monolayers and the behavior of a single layer. This would provide more detailed insights into how the thickness of MXene influences its radiative heat transfer capabilities.

The second part of the thesis examines the near-field radiative response of Cobalt Slanted Columnar Thin Films (Co-SCTF). These films were fabricated using glancing angle deposition, a technique that allows for the formation of nanostructured surfaces with specific geometric configurations. Generalized ellipsometry was used to determine the geometric structure and anisotropic dielectric properties of the Co-SCTF over the near-infrared to mid-infrared range.

The research showed that the NFRHT magnitudes between Co-SCTF exhibited a periodic trend over an in-plane rotation of the films. This periodicity varied with the gap distance between the films, allowing for better interaction of localized modes from the nanostructures. Theoretical calculations indicated that the NFRHT between Co-SCTF could reach higher magnitudes than those observed in dielectric materials, highlighting the potential of these nanostructured surfaces in advanced thermal applications.

Further research on the structural and material properties of Co-SCTF should include the effects of using semiconductor materials like silicon. Additionally, exploring other geometric structures such as boomerangs and zigzag shapes could provide insights into how these parameters influence radiative heat transfer. The intrinsic properties of semiconductors suggest that such studies could reveal even higher magnitudes of radiative heat flux exchange, enhancing the potential applications of these materials in thermal management technologies.

This research contributes to the growing body of knowledge on how 2D materials and nanostructures can be used to manipulate thermal radiation at the nanoscale. The findings suggest that the unique properties of Titanium Carbide MXene and Co-SCTF can be harnessed to

control radiative heat transfer in ways that were not previously possible with conventional materials. This has implications for the development of more efficient thermal management systems in electronic devices, as well as for other applications where precise control of heat transfer is essential.

REFERENCES

[1] Zhang, Z. M., 2020, *Nano/Microscale Heat Transfer*, Springer International Publishing, Cham.

[2] Song, B., Fiorino, A., Meyhofer, E., and Reddy, P., 2015, "Near-Field Radiative Thermal Transport: From Theory to Experiment," AIP Advances, **5**(5), p. 053503.

[3] 2013, *Radiative Heat Transfer*.

[4] Howell, J. R., Menguc, M. P., and Siegel, R., 2010, *Thermal Radiation Heat Transfer*, CRC Press, Boca Raton.

[5] *Principles of Statistical Radiophysics 3*.

[6] Joulain, K., Mulet, J.-P., Marquier, F., Carminati, R., and Greffet, J.-J., 2005, "Surface Electromagnetic Waves Thermally Excited: Radiative Heat Transfer, Coherence Properties and Casimir Forces Revisited in the near Field," Surface Science Reports, **57**(3), pp. 59–112.

[7] Pendry, J. B., 1999, "Radiative Exchange of Heat between Nanostructures," J. Phys.: Condens. Matter, **11**(35), p. 6621.

[8] Francoeur, M., 2018, "Near-Field Thermal Radiation," *Handbook of Thermal Science and Engineering*, Springer International Publishing, Cham, pp. 979–1021.

[9] Fu, C. J., and Zhang, Z. M., 2006, "Nanoscale Radiation Heat Transfer for Silicon at Different Doping Levels," International Journal of Heat and Mass Transfer, **49**(9), pp. 1703–1718.

[10] Francoeur, M., and Pinar Mengüç, M., 2008, "Role of Fluctuational Electrodynamics in Near-Field Radiative Heat Transfer," Journal of Quantitative Spectroscopy and Radiative Transfer, **109**(2), pp. 280–293.

[11] Rytov, S. M., 1959, *Theory of Electric Fluctuations and Thermal Radiation*, Air Force Cambridge Research Center.

[12] Song, J., Chen, L., Jin, L., Yao, L., Caglayan, H., and Hu, R., 2022, "hBN-Based Enhancement and Regulation of Radiative Heat Transfer between Two Monolayer Graphene Sheets," Appl. Phys. Lett., **121**(17), p. 171104.

[13] Wu, X., Fu, C., and Zhang, Z., 2018, "Influence of hBN Orientation on the Near-Field Radiative Heat Transfer between Graphene/hBN Heterostructures," JPE, **9**(3), p. 032702.

[14] Zhao, Q., Zhou, T., Wang, T., Liu, W., Liu, J., Yu, T., Liao, Q., and Liu, N., 2017, "Active Control of Near-Field Radiative Heat Transfer between Graphene-Covered Metamaterials," J. Phys. D: Appl. Phys., **50**(14), p. 145101.

[15] Huang, H., Shan, S., and Zhou, Z., 2022, "Enhanced Near-Field Thermal Radiation between Black Phosphorus with High Electron Density by BP/hBN Heterostructures," Nanoscale and Microscale Thermophysical Engineering, **0**(0), pp. 1–13.

[16] Xu, G., Sun, J., Mao, H., and Pan, T., 2020, "Near-Field Radiative Thermal Rectification Assisted by Black Phosphorus Sheets," International Journal of Thermal Sciences, **149**, p. 106179.

[17] Peng, J., Zhang, G., and Li, B., 2015, "Thermal Management in MoS2 Based Integrated Device Using Near-Field Radiation," Applied Physics Letters, **107**(13), p. 133108.

[18] Deng, M., Li, Z., Rong, X., Luo, Y., Li, B., Zheng, L., Wang, X., Lin, F., Meixner, A. J., Braun, K., Zhu, X., and Fang, Z., 2020, "Light-Controlled Near-Field Energy Transfer in Plasmonic Metasurface Coupled MoS2 Monolayer," Small, **16**(40), p. 2003539.

[19] Falkovsky, L. A., 2008, “Optical Properties of Graphene,” J. Phys.: Conf. Ser., **129**(1), p. 012004.
[20] “Super-Planckian Thermal Radiation Enabled by Coupled Quasi-Elliptic 2D Black Phosphorus Plasmons | Elsevier Enhanced Reader” [Online]. Available: https://reader.elsevier.com/reader/sd/pii/S1359431118328540?token=7642423DA4FE1FA1E95AF516E70771124C44CCBA48DECC981D017DEB308E90E025E705677A364892EFB6907E0A8C7D59&originRegion=us-east-1&originCreation=20230427232118. [Accessed: 27-Apr-2023].
[21] Lim, M., Lee, S. S., and Lee, B. J., 2013, “Near-Field Thermal Radiation between Graphene-Covered Doped Silicon Plates,” Opt. Express, OE, **21**(19), pp. 22173–22185.
[22] Wang, A., Zheng, Z., and Xuan, Y., 2016, “Near-Field Radiative Thermal Control with Graphene Covered on Different Materials,” Journal of Quantitative Spectroscopy and Radiative Transfer, **180**, pp. 117–125.
[23] Zhang, W. B., Wang, B. X., and Zhao, C. Y., 2022, “Active Control and Enhancement of Near-Field Heat Transfer between Dissimilar Materials by Strong Coupling Effects,” International Journal of Heat and Mass Transfer, **188**, p. 122588.
[24] Iqbal, N., Zhang, S., Wang, S., Fang, Z., Hu, Y., Dang, Y., Zhang, M., Jin, Y., Xu, J., Ju, B., and Ma, Y., 2023, “Measuring Near-Field Radiative Heat Transfer in a Graphene-$\mathrm{Si}\mathrm{C}$ Heterostructure,” Phys. Rev. Appl., **19**(2), p. 024019.
[25] Ge, L., Cang, Y., Gong, K., Zhou, L., Yu, D., and Luo, Y., 2018, “Control of Near-Field Radiative Heat Transfer Based on Anisotropic 2D Materials,” AIP Advances, **8**(8), p. 085321.
[26] Zhang, Y., Yi, H.-L., and Tan, H.-P., 2018, “Near-Field Radiative Heat Transfer between Black Phosphorus Sheets via Anisotropic Surface Plasmon Polaritons,” ACS Photonics, **5**(9), pp. 3739–3747.
[27] Peragut, F., Brubach, J.-B., Roy, P., and De Wilde, Y., 2014, “Infrared Near-Field Imaging and Spectroscopy Based on Thermal or Synchrotron Radiation,” Appl. Phys. Lett., **104**(25), p. 251118.
[28] Kittel, A., Wischnath, U. F., Welker, J., Huth, O., Rüting, F., and Biehs, S.-A., 2008, “Near-Field Thermal Imaging of Nanostructured Surfaces,” Applied Physics Letters, **93**(19), p. 193109.
[29] Li, Y., Li, W., Han, T., Zheng, X., Li, J., Li, B., Fan, S., and Qiu, C.-W., 2021, “Transforming Heat Transfer with Thermal Metamaterials and Devices,” Nat Rev Mater, **6**(6), pp. 488–507.
[30] Xiao, S., Wang, T., Liu, T., Zhou, C., Jiang, X., and Zhang, J., 2020, “Active Metamaterials and Metadevices: A Review,” J. Phys. D: Appl. Phys., **53**(50), p. 503002.
[31] Guo, Z., Jiang, H., and Chen, H., 2020, “Hyperbolic Metamaterials: From Dispersion Manipulation to Applications,” Journal of Applied Physics, **127**(7), p. 071101.
[32] Biehs, S.-A., and Ben-Abdallah, P., 2017, “Near-Field Heat Transfer between Multilayer Hyperbolic Metamaterials,” Zeitschrift für Naturforschung A, **72**(2), pp. 115–127.
[33] Ahamad, M. A., Inam, F. A., and Castelletto, S., 2023, “Silicon Carbide Metasurfaces for Controlling the Spontaneous Emission of Embedded Color Centers.”
[34] Cui, G.-C., Zhou, C.-L., Zhang, Y., and Yi, H.-L., 2023, “Significant Enhancement of Near-Field Radiative Heat Transfer by Misaligned Bilayer Heterostructure of Graphene-Covered Gratings,” ASME Journal of Heat and Mass Transfer, **146**(022801).

[35] Fernández-Hurtado, V., García-Vidal, F. J., Fan, S., and Cuevas, J. C., 2017, "Enhancing Near-Field Radiative Heat Transfer with Si-Based Metasurfaces," Phys. Rev. Lett., **118**(20), p. 203901.
[36] Iizuka, H., and Fan, S., 2018, "Significant Enhancement of Near-Field Electromagnetic Heat Transfer in a Multilayer Structure through Multiple Surface-States Coupling," Phys. Rev. Lett., **120**(6), p. 063901.
[37] Low, T., Rodin, A. S., Carvalho, A., Jiang, Y., Wang, H., Xia, F., and Castro Neto, A. H., 2014, "Tunable Optical Properties of Multilayer Black Phosphorus Thin Films," Phys. Rev. B, **90**(7), p. 075434.
[38] Qiao, J., Kong, X., Hu, Z.-X., Yang, F., and Ji, W., 2014, "High-Mobility Transport Anisotropy and Linear Dichroism in Few-Layer Black Phosphorus," Nat Commun, **5**(1), p. 4475.
[39] Han, M. Y., Özyilmaz, B., Zhang, Y., and Kim, P., 2007, "Energy Band-Gap Engineering of Graphene Nanoribbons," Phys. Rev. Lett., **98**(20), p. 206805.
[40] Li, L., Kim, J., Jin, C., Ye, G. J., Qiu, D. Y., da Jornada, F. H., Shi, Z., Chen, L., Zhang, Z., Yang, F., Watanabe, K., Taniguchi, T., Ren, W., Louie, S. G., Chen, X. H., Zhang, Y., and Wang, F., 2017, "Direct Observation of the Layer-Dependent Electronic Structure in Phosphorene," Nature Nanotech, **12**(1), pp. 21–25.
[41] Zanella, I., Guerini, S., Fagan, S. B., Mendes Filho, J., and Souza Filho, A. G., 2008, "Chemical Doping-Induced Gap Opening and Spin Polarization in Graphene," Phys. Rev. B, **77**(7), p. 073404.
[42] Kilic, U., Traouli, Y., Hilfiker, M., Bryant, K., Schoeche, S., Feder, R., Argyropoulos, C., Schubert, E., and Schubert, M., 2023, "Nanocolumnar Material Platforms:Universal Structural Parameters Revealed from Optical Anisotropy."
[43] Kılıç, U., Mock, A., Feder, R., Sekora, D., Hilfiker, M., Korlacki, R., Schubert, E., Argyropoulos, C., and Schubert, M., 2019, "Tunable Plasmonic Resonances in Si-Au Slanted Columnar Heterostructure Thin Films," Sci Rep, **9**(1), p. 71.
[44] Rice, C., Mock, A., Sekora, D., Schmidt, D., Hofmann, T., Schubert, E., and Schubert, M., 2017, "Control of Slanting Angle, Porosity, and Anisotropic Optical Constants of Slanted Columnar Thin Films via in Situ Nucleation Layer Tailoring," Applied Surface Science, **421**, pp. 766–771.
[45] Francoeur, M., Pinar Mengüç, M., and Vaillon, R., 2009, "Solution of Near-Field Thermal Radiation in One-Dimensional Layered Media Using Dyadic Green's Functions and the Scattering Matrix Method," Journal of Quantitative Spectroscopy and Radiative Transfer, **110**(18), pp. 2002–2018.
[46] Mulet, J.-P., Joulain, K., Carminati, R., and Greffet, J.-J., 2002, "Enhanced Radiative Heat Transfer at Nanometric Distances," Microscale Thermophysical Engineering, **6**(3), pp. 209–222.
[47] Francoeur, M., Mengüç, M. P., and Vaillon, R., 2010, "Spectral Tuning of Near-Field Radiative Heat Flux between Two Thin Silicon Carbide Films," J. Phys. D: Appl. Phys., **43**(7), p. 075501.
[48] Yeh, P., 2004, *Optical Waves in Layered Media*, Wiley.
[49] Ko, D. Y. K., and Sambles, J. R., 1988, "Scattering Matrix Method for Propagation of Radiation in Stratified Media: Attenuated Total Reflection Studies of Liquid Crystals," J. Opt. Soc. Am. A, **5**(11), p. 1863.

[50] Whittaker, D. M., and Culshaw, I. S., 1999, “Scattering-Matrix Treatment of Patterned Multilayer Photonic Structures,” Phys. Rev. B, **60**(4), pp. 2610–2618.
[51] Rosa, F. S. S., Dalvit, D. A. R., and Milonni, P. W., 2008, “Casimir Interactions for Anisotropic Magnetodielectric Metamaterials,” Phys. Rev. A, **78**(3), p. 032117.
[52] Biehs, S.-A., Ben-Abdallah, P., Rosa, F. S. S., Joulain, K., and Greffet, J.-J., 2011, “Nanoscale Heat Flux between Nanoporous Materials,” Opt. Express, OE, **19**(105), pp. A1088–A1103.
[53] Hu, L., Narayanaswamy, A., Chen, X., and Chen, G., 2008, “Near-Field Thermal Radiation between Two Closely Spaced Glass Plates Exceeding Planck’s Blackbody Radiation Law,” Applied Physics Letters, **92**(13), p. 133106.
[54] Chen, L., Song, J., Jin, L., Yao, X., Zhao, H., and Cheng, Q., 2023, “Regulation of Near-Field Radiative Heat Transfer between Multilayer BP/hBN Heterostructures,” Langmuir, **39**(36), pp. 12817–12825.
[55] Ontiveros, D., Viñes, F., and Sousa, C., 2023, “Bandgap Engineering of MXene Compounds for Water Splitting,” J. Mater. Chem. A, **11**(25), pp. 13754–13764.
[56] Cui, J., Peng, Q., Zhou, J., and Sun, Z., 2019, “Strain-Tunable Electronic Structures and Optical Properties of Semiconducting MXenes,” Nanotechnology, **30**(34), p. 345205.
[57] Zhang, P., Shou, H., Xia, Y., Wang, C., Wei, S., Xu, W., Chen, Y., Liu, Z., Guo, X., Zhu, K., Cao, Y., Wu, X., Chen, S., and Song, L., 2023, “X-Ray Insights into Formation of −O Functional Groups on MXenes: Two-Step Dehydrogenation of Adsorbed Water,” Nano Letters.
[58] Zhang, N., Zhang, J., Zhu, X., Yuan, S., Wang, D., Xu, H., and Wang, Z., 2024, “Synergistic Effect of Ti3C2Tx MXene Nanosheets and Tannic Acid–Fe3+ Network in Constructing High-Performance Hydrogel Composite Membrane for Photothermal Membrane Distillation,” Nano Letters.
[59] Zhang, D., Shah, D., Boltasseva, A., and Gogotsi, Y., 2022, “MXenes for Photonics,” ACS Photonics, **9**(4), pp. 1108–1116.
[60] Lin, H., Wang, X., Yu, L., Chen, Y., and Shi, J., 2016, “Two-Dimensional Ultrathin MXene Ceramic Nanosheets for Photothermal Conversion,” ACS Publications [Online]. Available: https://pubs.acs.org/doi/full/10.1021/acs.nanolett.6b04339. [Accessed: 19-Jul-2024].
[61] Mauchamp, V., Bugnet, M., Bellido, E. P., Botton, G. A., Moreau, P., Magne, D., Naguib, M., Cabioc’h, T., and Barsoum, M. W., 2014, “Enhanced and Tunable Surface Plasmons in Two-Dimensional ${\mathrm{Ti}}_{3}{\mathrm{C}}_{2}$ Stacks: Electronic Structure versus Boundary Effects,” Phys. Rev. B, **89**(23), p. 235428.
[62] Limbu, T. B., Chitara, B., Garcia Cervantes, M. Y., Zhou, Y., Huang, S., Tang, Y., and Yan, F., 2020, “Unravelling the Thickness Dependence and Mechanism of Surface-Enhanced Raman Scattering on Ti3C2TX MXene Nanosheets,” J. Phys. Chem. C, **124**(32), pp. 17772–17782.
[63] Li, L., Shi, M., Liu, X., Jin, X., Cao, Y., Yang, Y., Wang, W., and Wang, J., 2021, “Ultrathin Titanium Carbide (MXene) Films for High-Temperature Thermal Camouflage,” Advanced Functional Materials, **31**(35), p. 2101381.
[64] Zhao, Y., Deng, C., Yan, B., Yang, Q., Gu, Y., Guo, R., Lan, J., and Chen, S., 2023, “One-Step Method for Fabricating Janus Aramid Nanofiber/MXene Nanocomposite Films with Improved Joule Heating and Thermal Camouflage Properties,” ACS Appl. Mater. Interfaces, **15**(47), pp. 55150–55162.
[65] Palik, E. D., 1998, *Handbook of Optical Constants of Solids*, Academic Press.

[66] Rincón-García, L., Thompson, D., Mittapally, R., Agraït, N., Meyhofer, E., and Reddy, P., 2022, "Enhancement and Saturation of Near-Field Radiative Heat Transfer in Nanogaps between Metallic Surfaces," Phys. Rev. Lett., **129**(14), p. 145901.
[67] Khayam, S., and Ghashami, M., 2024, "Enhancement and Suppression of Near-Field Radiative Heat Transfer in Planar Many-Body Systems," Phys. Rev. B, **110**(3), p. 035412.
[68] Shi, K., Bao, F., and He, S., 2017, "Enhanced Near-Field Thermal Radiation Based on Multilayer Graphene-hBN Heterostructures," ACS Photonics, **4**(4), pp. 971–978.
[69] Robbie, K., and Brett, M. J., 1997, "Sculptured Thin Films and Glancing Angle Deposition: Growth Mechanics and Applications," Journal of Vacuum Science & Technology A, **15**(3), pp. 1460–1465.
[70] Hawkeye, M. M., and Brett, M. J., 2007, "Glancing Angle Deposition: Fabrication, Properties, and Applications of Micro- and Nanostructured Thin Films," Journal of Vacuum Science & Technology A, **25**(5), pp. 1317–1335.
[71] Hawkeye, M. M., Taschuk, M. T., and Brett, M. J., 2014, *Glancing Angle Deposition of Thin Films: Engineering the Nanoscale*, John Wiley & Sons.
[72] Schmidt, D., Kjerstad, A. C., Hofmann, T., Skomski, R., Schubert, E., and Schubert, M., 2009, "Optical, Structural, and Magnetic Properties of Cobalt Nanostructure Thin Films," Journal of Applied Physics, **105**(11), p. 113508.
[73] Hofmann, T., Schmidt, D., Boosalis, A., Kühne, P., Skomski, R., Herzinger, C. M., Woollam, J. A., Schubert, M., and Schubert, E., 2011, "THz Dielectric Anisotropy of Metal Slanted Columnar Thin Films," Applied Physics Letters, **99**(8), p. 081903.
[74] Kilic, U., Hilfiker, M., Ruder, A., Feder, R., Schubert, E., Schubert, M., and Argyropoulos, C., 2021, "Broadband Enhanced Chirality with Tunable Response in Hybrid Plasmonic Helical Metamaterials," Advanced Functional Materials, **31**(20), p. 2010329.
[75] Abbasian, S., Moshaii, A., Vayghan, N. S., and Nikkhah, M., 2018, "Fabrication of Ag Nanostructures with Remarkable Narrow Plasmonic Resonances by Glancing Angle Deposition," Applied Surface Science, **441**, pp. 613–620.
[76] He, Y., Fu, J., and Zhao, Y., 2014, "Oblique Angle Deposition and Its Applications in Plasmonics," Front. Phys., **9**(1), pp. 47–59.
[77] Shalabney, A., Lakhtakia, A., Abdulhalim, I., Lahav, A., Patzig, C., Hazek, I., Karabchevsky, A., Rauschenbach, B., Zhang, F., and Xu, J., 2009, "Surface Plasmon Resonance from Metallic Columnar Thin Films," Photonics and Nanostructures - Fundamentals and Applications, **7**(4), pp. 176–185.
[78] Díaz-Núñez, P., García-Martín, J. M., González, M. U., González-Arrabal, R., Rivera, A., Alonso-González, P., Martín-Sánchez, J., Taboada-Gutiérrez, J., González-Rubio, G., Guerrero-Martínez, A., Bañares, L., and Peña-Rodríguez, O., 2019, "On the Large Near-Field Enhancement on Nanocolumnar Gold Substrates," Sci Rep, **9**(1), p. 13933.
[79] Chu, Q., Zhong, F., Shang, X., Zhang, Y., Zhu, S., and Liu, H., 2024, "Controlling Thermal Emission with Metasurfaces and Its Applications," Nanophotonics, **13**(8), pp. 1279–1301.
[80] Mascaretti, L., Chen, Y., Henrotte, O., Yesilyurt, O., Shalaev, V. M., Naldoni, A., and Boltasseva, A., 2023, "Designing Metasurfaces for Efficient Solar Energy Conversion," ACS Photonics, **10**(12), pp. 4079–4103.
[81] Schmidt, D., Schubert, E., and Schubert, M., 2013, "Generalized Ellipsometry Characterization of Sculptured Thin Films Made by Glancing Angle Deposition," *Ellipsometry at the Nanoscale*, M. Losurdo, and K. Hingerl, eds., Springer, Berlin, Heidelberg, pp. 341–410.

[82] Fujiwara, H., 2007, *Spectroscopic Ellipsometry: Principles and Applications*, John Wiley & Sons.
[83] Gish, D. A., Nsiah, F., McDermott, M. T., and Brett, M. J., 2007, "Localized Surface Plasmon Resonance Biosensor Using Silver Nanostructures Fabricated by Glancing Angle Deposition," Anal. Chem., **79**(11), pp. 4228–4232.
[84] Lakhtakia, A., 2002, "Sculptured Thin Films: Accomplishments and Emerging Uses," Materials Science and Engineering: C, **19**(1), pp. 427–434.
[85] Savaloni, H., Fakharpour, M., Siabi-Garjan, A., Placido, F., and Babaei, F., 2017, "Nano-Structure and Optical Properties (Plasmonic) of Graded Helical Square Tower-like (Terraced) Mn Sculptured Thin Films," Applied Surface Science, **393**, pp. 234–255.
[86] Schmidt, D., Hofmann, T., Herzinger, C. M., Schubert, E., and Schubert, M., 2010, "Magneto-Optical Properties of Cobalt Slanted Columnar Thin Films," Applied Physics Letters, **96**(9), p. 091906.